

Article

Progressive Fracture Behavior and Acoustic Emission Release of CJBs Affected by Joint Distance Ratio

Yongyi Wang ¹, Bin Gong ^{2,*}, Yongjun Zhang ³, Xiaoyu Yang ⁴ and Chun'an Tang ¹

¹ State Key Laboratory of Coastal and Offshore Engineering, Dalian University of Technology, Dalian 116024, China

² College of Engineering, Design and Physical Sciences, Brunel University London, London UB8 3PH, UK

³ School of Civil Engineering, Qingdao University of Technology, Qingdao 266520, China

⁴ School of Civil Engineering, Chongqing Jiaotong University, Chongqing 400074, China

* Correspondence: bin.gong@brunel.ac.uk

Abstract: The progressive collapse behavior and energy release of columnar jointed basalts (CJBs) can be greatly influenced by different joint distance ratios. By adopting the digital image correlation, a series of heterogeneous CJB models are established. The continuous fracture process and acoustic emissions (AEs) are captured numerically under varying lateral pressures. The load curves under different joint distance ratios and model boundaries are analyzed. Meanwhile, the strength, deformation modulus and AE rule are discussed. The data indicate that under plane strain, the troughs of compression strength appear at the column dip angle $\beta = 30^\circ, 150^\circ, 210^\circ$ or 330° ; the equivalent deformation modulus changes in an elliptical way with β increasing; the compression strength and equivalent deformation modulus are higher than the case between plane stress and plane strain under different joint distance ratios. When $\beta = 30^\circ$, the accumulation of AE energy corresponding to the stress peak under plane strain are higher than the case between plane stress and plane strain but becomes lower when β increases to 60° , which implies the critical transformation of the AE energy-related failure precursor affected by column dip angle. These achievements will contribute to the design, construction and support of slopes and tunnels encountering CJBs.

Keywords: columnar jointed basalt; failure mechanism; acoustic emission; joint distance ratio; numerical simulation

MSC: 74-10



Citation: Wang, Y.; Gong, B.; Zhang, Y.; Yang, X.; Tang, C. Progressive Fracture Behavior and Acoustic Emission Release of CJBs Affected by Joint Distance Ratio. *Mathematics* **2022**, *10*, 4149. <https://doi.org/10.3390/math10214149>

Academic Editors: Danial Jahed Armaghani, Hadi Khabbaz, Manoj Khandelwal, Niaz Muhammad Shahani and Ramesh Murlidhar Bhatawdekar

Received: 19 October 2022

Accepted: 3 November 2022

Published: 6 November 2022

Publisher's Note: MDPI stays neutral with regard to jurisdictional claims in published maps and institutional affiliations.



Copyright: © 2022 by the authors. Licensee MDPI, Basel, Switzerland. This article is an open access article distributed under the terms and conditions of the Creative Commons Attribution (CC BY) license (<https://creativecommons.org/licenses/by/4.0/>).

1. Introduction

The columnar jointed basalts (CJBs) generally form because of the condensation and contraction of magma and contain obvious columnar joints. The CJBs are popularly distributed in many sites on this planet, such as Scotland, Siberia, China, Mexico, Australia, the United States, Brazil, India, etc. [1–4]. Columnar joints have even been found on Mars [5]. In the past decades, the columnar jointed rock masses (CJRMs) were encountered in several hydropower stations located in southwest China, such as the Baihetan, Jinanqiao, Wudongde, Xiluodu, and Tongjiezi hydropower stations. Two photographs [5,6] of CJRMs are shown in Figure 1.

Some researchers have investigated the anisotropy, size effect and confining pressure effect of CJBs (or CJRMs). In terms of numerical simulation, insightful achievements have been obtained. However, few studies have been conducted regarding the mechanical responses of CJBs with different joint distance ratios and model boundaries. The homogenization-based model was developed by Meng et al. [7] for studying the effect of discontinuous structures and the elastic parameters. Zheng et al. [1] calculated the influences of size effect and anisotropy using the discrete element method (DEM). Yan et al. [8] modelled the deformation and failure of CJRMs using the finite difference method (FDM).

Li et al. [3] discussed the transient-thermoelastic fractures affected by the highly time-dependent thermal loads by applying the numerical manifold method (NMM). Niu et al. [9] calculated the permeability property of CJRMs with various dip angles numerically, and a case study was also carried out. However, the gradual failure process and energy evolution of CJBs have not been understood in depth.

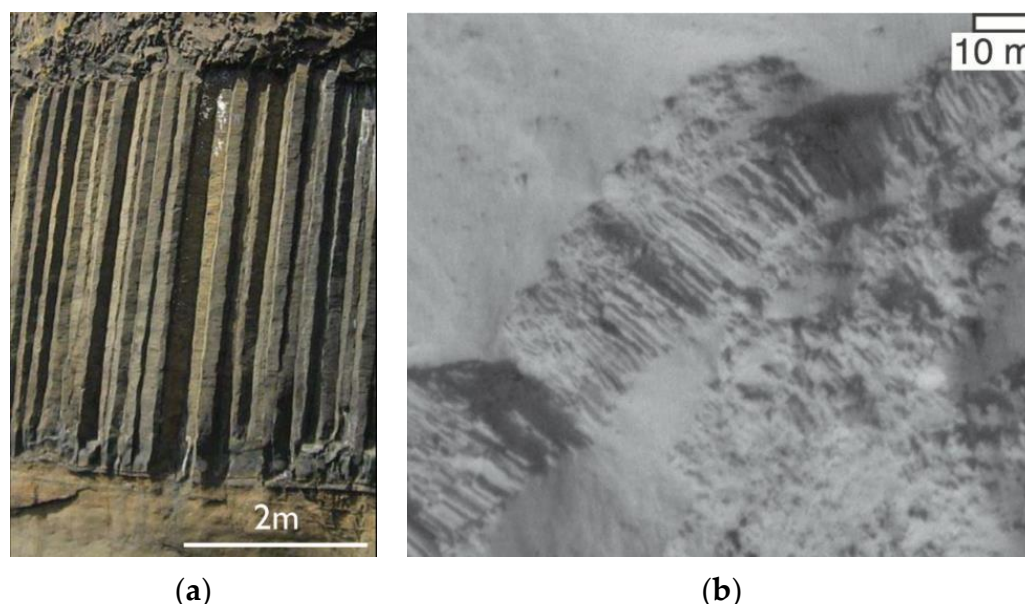


Figure 1. The columnar jointed rock masses observed in field: (a) Fingal's Cave on Staffa in Scotland [6]; (b) the columnar joints discovered on Mars [5].

In terms of physical tests, some useful results have been achieved. With the aim of understanding the hydraulic fracturing of CJRMs, the compression tests were performed under triaxial stress state by Xiang et al. [10]. Through a series of compression experiments under uniaxial stress state, Ke et al. [11] analyzed the anisotropy induced by transverse joints. Shi et al. [12] presented an approach to obtain the strengths using the Mohr–Coulomb and Hoek–Brown criteria under triaxial stresses. A group of laboratory tests were carried out by Jin et al. [4] for understanding the anisotropic parameters of CJRMs. To analyze the actual geological structures on site, the uniaxial testing was carried out by Ji et al. [13]. The quadrangular, pentagonal and hexagonal prisms were also investigated by Que et al. [14] in a laboratory. The anisotropic parameters were discussed by combining the structural features of three kinds of models. In the field tests of CJBs (or CJRMs), many valuable results have been obtained. However, the rock masses in nature are generally complicated. The preparation of rock specimens would suffer unexpected disturbance [2,15–19]. Meanwhile, the AE energy evolution during the fracture process for the CJBs are greatly affected by joint distance ratio and model boundary and remains unclear. Moreover, when there are many experimental scheme configurations and specimens, time-consuming and uneconomical problems will be encountered.

On the one hand, the influence of column dip angles, joint distance ratios and model boundaries on the mechanical properties of CJBs should be revealed systematically. On the other hand, it will contribute to understand the collapse mechanism to reproduce the progressive fracture process and AE energy evolution appropriately. In the engineering projects, the CJBs could not only show significant discontinuity and anisotropy, but also suffer lateral pressure. Hence, it has significant value to reveal the complex deforming and bearing features, failure mechanisms and instability precursor of CJBs under lateral pressure.

In this study, to analyze the failure mechanism and AE release rule of CJBs containing various joint distance ratios under different boundary conditions, the digital CJB figures were used for creating the non-homogeneous models. Based on meso-mechanics and

statistical damage mechanics, a series of numerical tests were conducted. The simulated results were analyzed by comparing with the corresponding tests to verify the rationality and reliability. Furthermore, the continuous failure process and damage failure pattern of the CJB were reproduced. The influence of column dip angles, joint distance ratios and model boundaries on the accumulation of AE energy were comprehensively analyzed to provide the theoretical basis for the treatment measures.

2. Materials and Methods

2.1. The Combination of RFPA and DIC

In terms of the main advances of the rock failure process analysis (RFPA) approach, the assumptions on where and how cracks will occur and propagate are not needed [20,21]. In addition, its effectiveness in modelling the non-linear deforming and bearing of rocks has been verified by many researchers [22,23]. Moreover, RFPA has been adopted in simulating slope instability [24], size effect [25] and zonal disintegration characteristics [26] of rocks. Thus, RFPA has been chosen in this study.

The digital image correlation (DIC) was adopted for building up the RFPA models. Firstly, the vectorized coordinates of elements were obtained through importing and processing the digital figures using the gray-threshold segmentation. Considering the digital figures consist of many square pixels, each pixel corresponds to one finite element, and the spatial coordinates of every pixel corresponds to the node coordinates of the related element. Secondly, the joint or matrix of rocks can be determined by dividing the gray value of pixels, and the related material properties will be assigned. According to the above principle, the creation process of non-homogeneous numerical models is presented in Figure 2a.

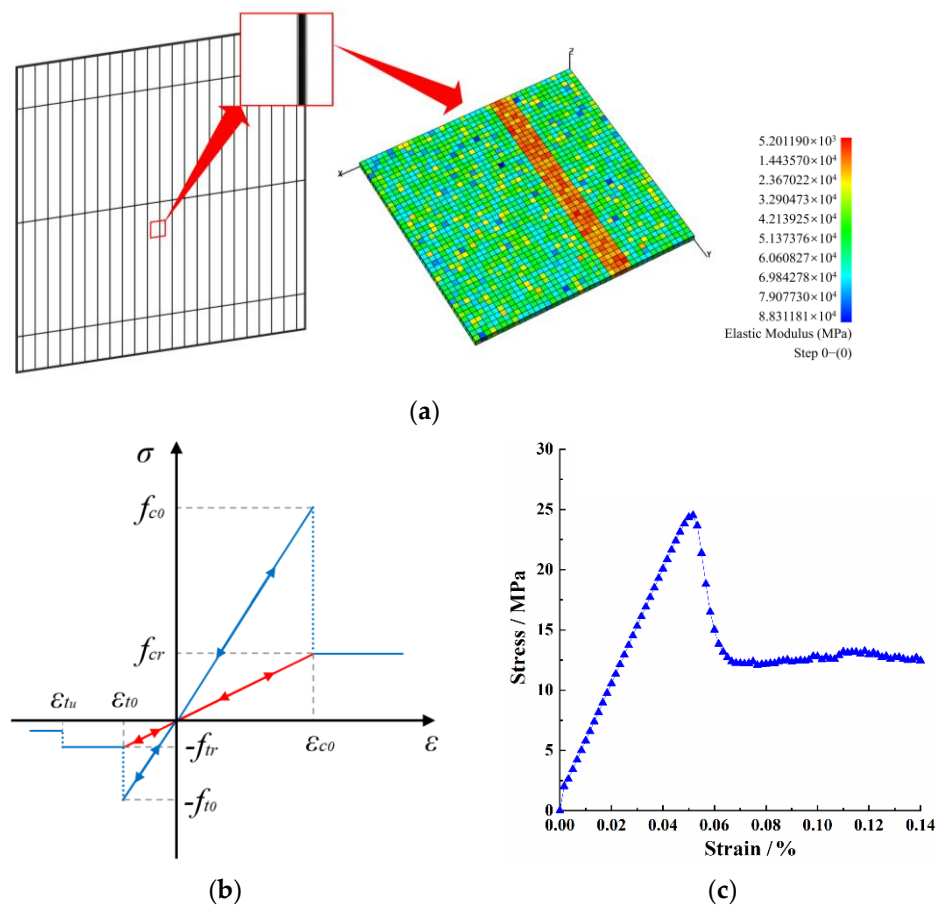


Figure 2. (a) The creation process of non-homogeneous numerical models; (b) the element constitution subject to uniaxial stress; (c) the stress-strain curve.

The element constitution subject to uniaxial stress is depicted in Figure 2b. Through the approach of extending uniaxial constitutive relation to triaxial stress states (Mazars and Pijaudier-Cabot [27]), the constitutive relation shown in Figure 2a can be extended to the triaxial stress states.

2.2. Damage and Failure of One Meso-Element

The rock nonuniformity can be taken into account if the parameter values of meso-elements are assumed to obey the Weibull distribution:

$$f(u) = \frac{m}{u_0} \left(\frac{u}{u_0} \right)^{m-1} \exp\left(-\frac{u}{u_0}\right)^m \quad (1)$$

where u is a certain parameter of meso-elements, e.g., compressive strength; u_0 represents the related mean value of u . The notation m represents the heterogeneity index and reflects the nonuniform degree. A higher m implies a higher non-uniformity.

If one element suffers tension along an axis, the elastic-brittle damage constitution described by Equation (2) will be applied.

$$\sigma_3 \leq f_t \quad (2)$$

where f_t represents the unique strength under uniaxial tensile. Note that the stress and strain under compression are positive in this study.

Moreover, the Mohr-Coulomb strength criterion is used for judging the shear damage of one meso-element as shown by Equation (3).

$$\sigma_1 - \frac{1 + \sin\varphi}{1 - \sin\varphi} \sigma_3 - f_c \geq 0 \quad (3)$$

where σ_1 , σ_3 , φ and f_c represents the major principal stress, minor principal stress, internal friction angle and uniaxial compressive strength, respectively. The damage-induced degeneration of element parameter can be computed according to Wang et al. (2022) [28].

2.3. Modeling Effectiveness

The indoor experiment by Ke et al. [11] is adopted to verify the simulation-based approach. Ke et al. [11] made the columns using cement, fine sand, water and water reducer with the mass ratio of 1.0:0.5:0.35:0.002. A regular hexagonal prism containing the section diameter = 10 mm and the length = 50 mm was selected for simulating the actual column. The white cement slurry was used for bonding columns, which simulates joint surface. The ratio of longitudinal to transverse of column was 5. The shift distance of transverse joint was 25 mm. Seven kinds of column-dip angles (β) from 0° to 90° were considered. The rock mass specimens were regular 50 mm \times 50 mm \times 100 mm quadrangular prisms. The compressive testing was carried out by applying the CSS-3940YJ rock mechanics servo testing machine. The loading method with constant displacement rate of 0.05 mm/min was used. A flat steel cushion block was placed at the rock ends. Then, vertical pressure was applied until the failure of the specimen.

Note that the 50 mm \times 100 mm models were used for verification under different load directions subject to plane strain. The inner hexagonal prisms have a diameter of 10 mm. The digital figures were used for creating the numerical samples as displayed in Table 1. The parameter values of the finite element models were determined according to the literatures [8–13,16–19] and presented in Table 2. The displacement load with a ratio of 0.005 mm/step was used until the model failure.

Table 1. The model geometry and load conditions used for verification.

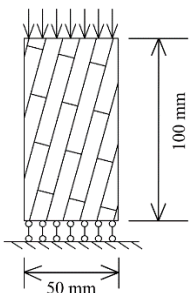
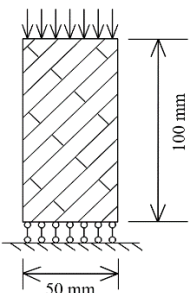
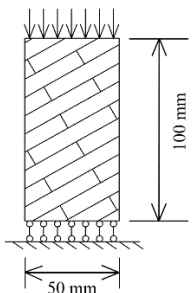
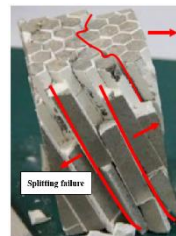


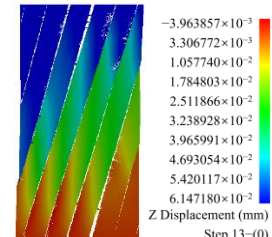
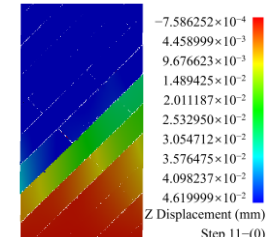
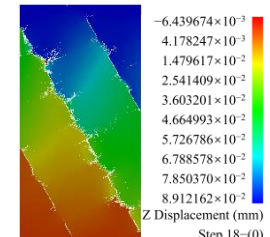
Column Dip Angle (β)	15°	45°	60°
Model			

Table 2. The physical-mechanical parameter values for numerical simulation.

Material Type	Heterogeneity Index	Elastic Modulus (GPa)	Uniaxial Compressive Strength (MPa)	Poisson's Ratio	Friction Angle (°)
Basalt	5	60	120	0.2	56.15
Joint	5	15	30	0.25	36

Table 3 shows the related comparison of the specimen failure modes obtained by simulations and experiments. We can see that the results when $\beta = 15^\circ$ and $\beta = 45^\circ$ in numerical and laboratory physical tests show relatively good similarity. However, for the condition of $\beta = 60^\circ$, there are certain differences between them. This is because of the end effect of the specimen in laboratory test. Namely, there is a certain friction constraint at the ends of both sides of the specimen in laboratory test.

Table 3. The failure modes obtained by simulation and experiment [11].

Column Dip Angle (β)	15°	45°	60°
Experiment [11]			
Simulation			

2.4. Numerical Investigation

In this section, the column length and diameter are 0.5~3 m and 13~25 cm, respectively. The specimens for numerical testing are square models and are 4 m in size, and the diameter of columns inside specimens is 20 cm. The rock heterogeneity index is considered as 5. The elastic modulus of joints is 15 GPa. The residual index of strengths after rock failure is taken as 0.5. The dip angles of the column are 0°, 15°, 30°, 45°, 60°, 75° and 90°, respectively. The

spacing of the secondary joints is 1.5 m. Simultaneously, the distance ratio of the secondary joints changes from 0% to 50%. The lateral pressure is considered as 4 MPa. In terms of the boundary conditions, two cases are taken into account including the plane strain and the case between plane stress and plane strain.

Moreover, the meso-element size of the models remains the same. For instance, the element number of the 4 m specimen is 1,081,600. The applied configuration for established CJB specimens along the direction parallel to the column axis are presented as Figure 3a–g. For Figure 3e, the normal displacement constraints are applied on the two faces. For Figure 3f, the normal displacement constraint is applied only on one face, and the other normal direction of the plane is free. For Figure 3a–g, the pre-set loading is applied onto the top surface along the vertical direction until the model failure.

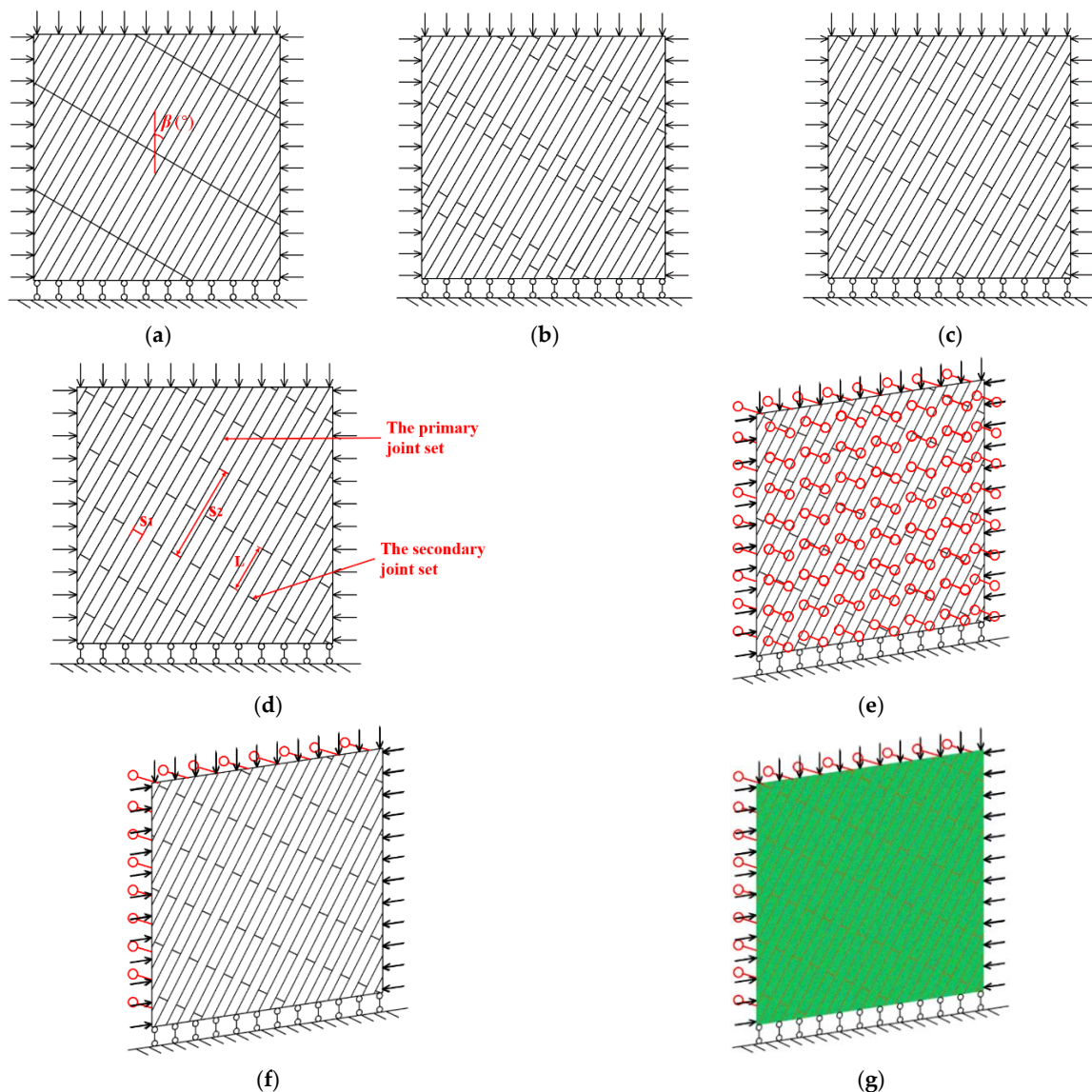


Figure 3. (a–d) The CJBs containing the joint distance ratios 0%, 20%, 40% and 50%, respectively; (e) the model setup under plane strain; (f,g) the model setup for the case between plane stress and plane strain.

Generally, the parameter values of joints will be lower than rock matrix [29]. The selection of parameters can affect the elastic moduli and compression strengths [30]. According to the corresponding literatures [8–13,16–19], the mechanical parameter values of rock and joint of CJBs are determined (see Table 2).

3. Results

3.1. The Deforming and Bearing under Different Joint Distance Ratios

3.1.1. Under Plane Strain

According to Figure 4a, under the lateral pressure of 4 MPa, in terms of compressive strength (CS), when the joint distance ratio is 0%, the compressive strength of specimen shows a roughly U-shaped trend as β increases; when the joint distance ratio is 20%, 40% and 50%, that changes roughly in a V-shaped trend as β increases. At β of 60° and 75°, compared with the specimen with a joint distance ratio of 0%, for the models with the joint distance ratios of 20%, 40% and 50%, the CS is risen greatly, which is caused by the obvious growth of the effective bearing area. Furthermore, combined with Figure 4c, it is clear that for the CJBs with various joint distance ratios, the troughs of CS appear at $\beta = 30^\circ, 150^\circ, 210^\circ$ and 330° ; the peaks of CS appear at $\beta = 0^\circ, 90^\circ, 180^\circ$ and 270° . Additionally, for the CJBs with the joint distance ratios of 20%~50%, the CSs of specimens decrease sharply near $\beta = 0^\circ$ and 180° , which results from the rapid penetration failure of joints. However, they change relatively gently near $\beta = 90^\circ$ and 270° .

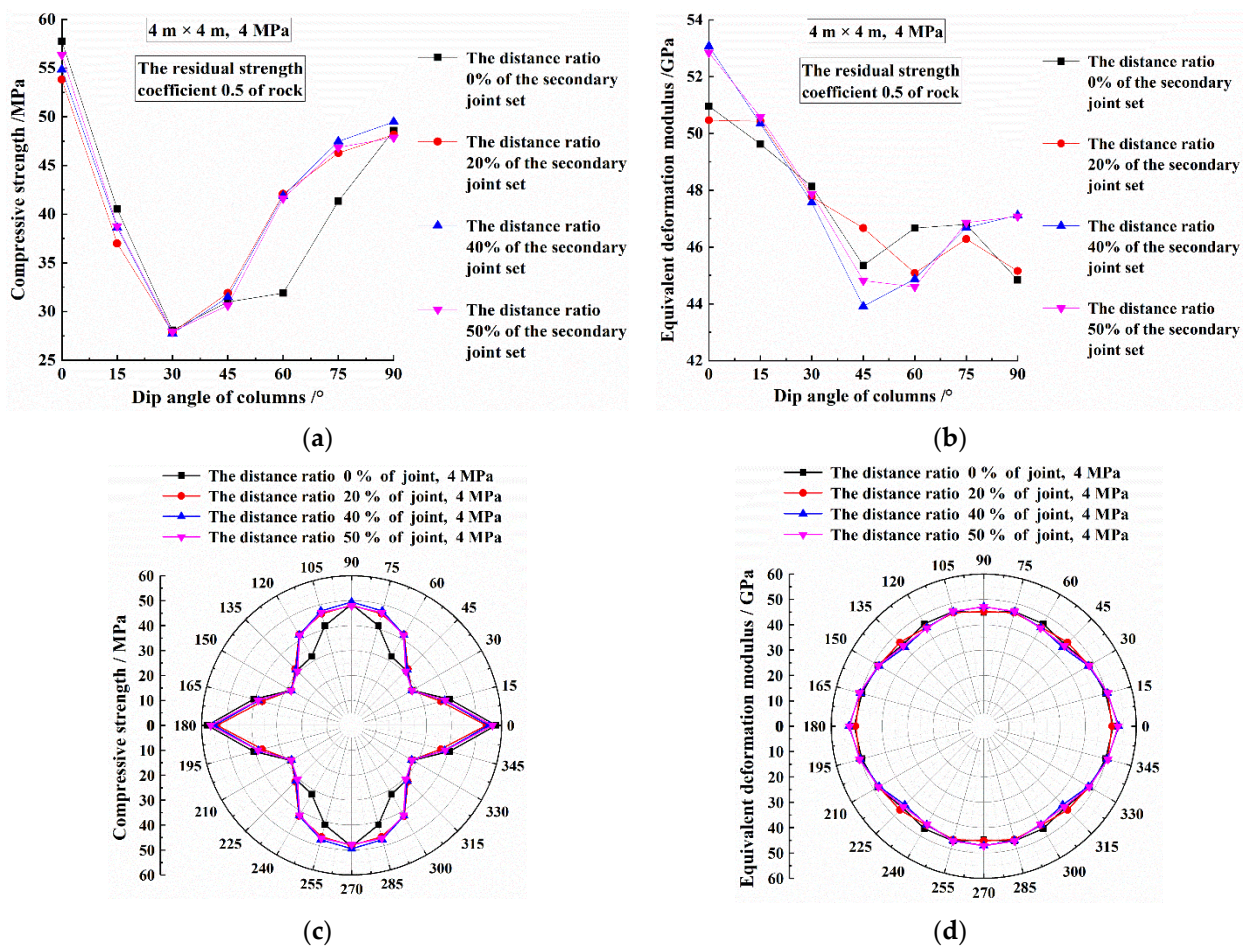


Figure 4. The CJBs with different joint distance ratios: (a,c) the compressive strength; (b,d) the equivalent deformation modulus.

Figure 4b shows that under plane strain, in the aspect of equivalent deformation modulus (EDM), when the joint distance ratio is 0%~50%, the EDM of specimen reduces in the beginning, but changes/fluctuates with β increases later. The highest value of EDM appears when $\beta = 0^\circ$; the lower values of EDM exist at the range of $\beta = 45^\circ \sim 90^\circ$. Moreover, combined with Figure 4d, it is clear that for the CJBs with various joint distance ratios, the EDMs change in elliptical way with β increases. The EDM of the models is less sensitive to

the variation in joint distance ratio, which is mainly because the compaction and elastic deformation are not sensitive to joint distance ratio.

Figure 5a,b displays the loading curves of the CJBs owning various joint distance ratios when the lateral pressure = 4 MPa under plane strain. As presented in Figure 5a, when the joint distance ratio = 0%, the loading curve of the CJBs with $\beta = 60^\circ$ show ductile failure characteristic, while the loading curves of other CJBs show basically brittle failure characteristics. In addition, no residual strength stage exists on the loading curves for $\beta = 15^\circ, 30^\circ$ and 75° , indicating that the failure and overall instability of specimen occur. As shown in Figure 5b,d, the loading curves for various column dip angles are almost with some characteristics of brittle failure. When the joint distance ratio is 20%, 40% and 50%, there is no residual strength stage in the loading curve when $\beta = 15^\circ$, while regarding the other column dip angles, the residual strength stages exist in the loading curves. If $\beta = 30^\circ$ and 75° , compared with the CJBs with joint distance ratio 0%, for the CJBs with joint distance ratios 20%~50%, the residual strength stability is improved.

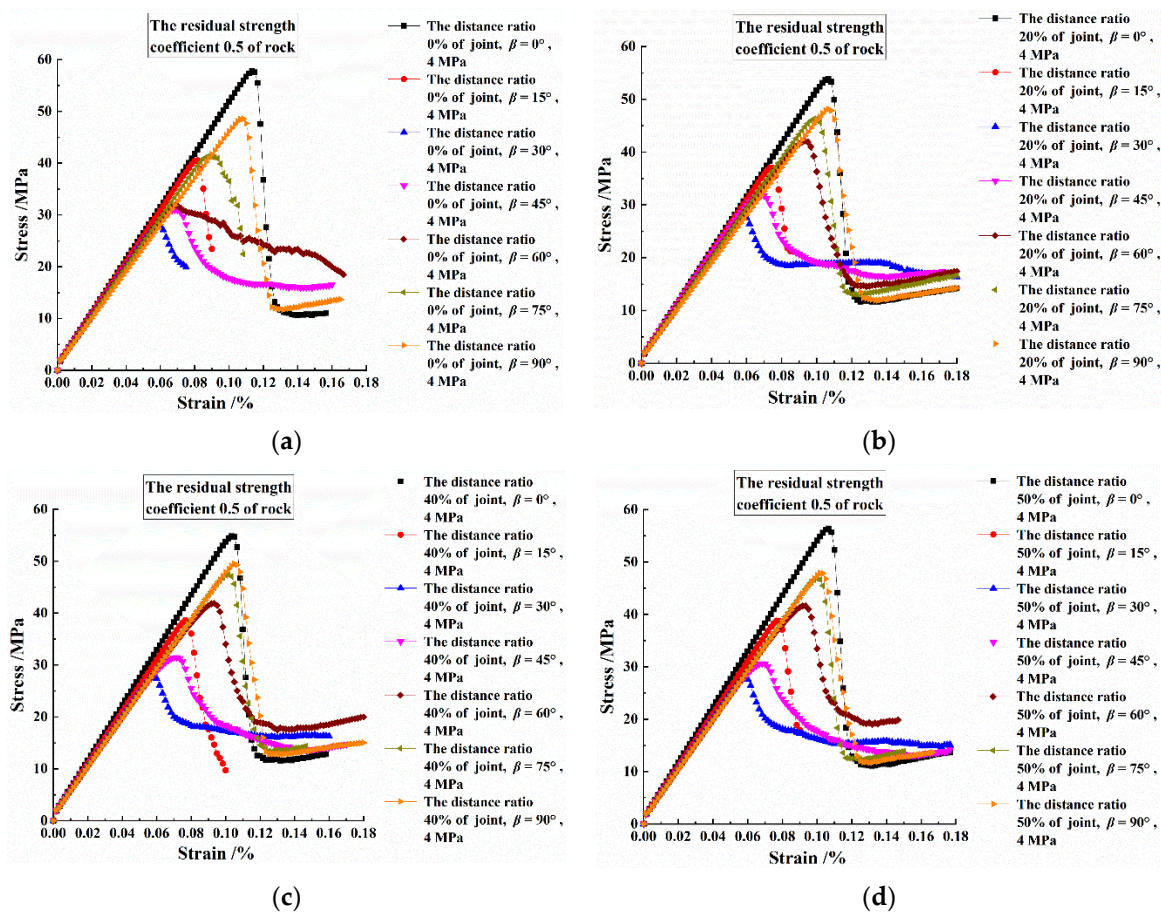


Figure 5. The loading curves of CJBs: (a) the joint distance ratio of 0%; (b) the joint distance ratio of 20%; (c) the joint distance ratio of 40%; (d) for the joint distance ratio of 50%.

3.1.2. The Cases of Two Kinds of Model Boundaries

Figure 6 shows the CSs and EDMs of CJBs with different joint distance ratios in the cases of two kinds of model boundaries. As depicted in Figure 6a, in terms of CS, for the CJBs with $\beta = 30^\circ$ under the lateral pressure = 4 MPa, from the perspective of joint distance ratio, if the boundary condition is the case between plane stress and plane strain, the CS of specimen displays a decreasing and increasing fluctuation trend with the growth of joint distance ratio, in which the ratio of the highest CS to the lowest CS is 1.023, indicating the very small fluctuation range. If the boundary condition is plane strain, the model CS reduces in the beginning, but rises as the joint distance ratio increases later. The ratio of the

highest value to the lowest value of CS is 1.012, which shows that the variation range is also very small. From the perspective of model boundary condition, the CS under Case II is higher than Case I. If the model boundaries are changed in Case II, the increasing rates of CSs of specimens with joint distance ratios of 0%, 20%, 40% and 50% are 13.41%, 14.56%, 13.22% and 15.23%, respectively.

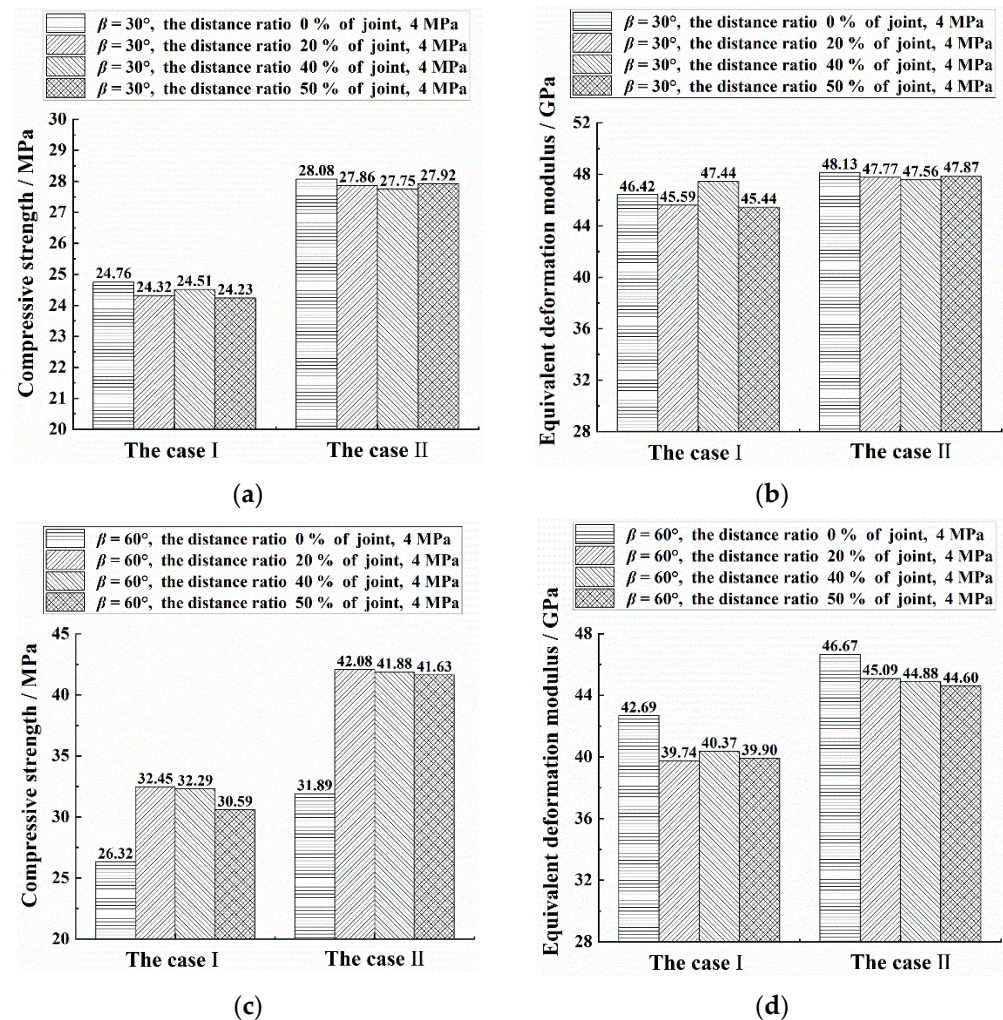


Figure 6. For the cases of two kinds of model boundaries and the CJBs with different joint distance ratios: (a,c) the compressive strength for $\beta = 30^\circ$ and 60° ; (b,d) the equivalent deformation modulus for $\beta = 30^\circ$ and 60° (Case I corresponding to the case between plane stress and plane strain and Case II corresponding to the plane strain).

As presented in Figure 6b, for the CJBs with $\beta = 30^\circ$ when the lateral pressure = 4 MPa, from the perspective of joint distance ratio, if the model boundaries are Case II, the EDM of specimen displays a reducing and rising fluctuation trend with the increase in joint distance ratio. If the model boundaries are Case I, the model EDM decreases in the beginning, but increases with the growth of joint distance ratio. From the perspective of model boundary condition, if the model boundaries vary from Case I to Case II, the increasing rates of EDMs of specimens with joint distance ratios of 0%, 20%, 40% and 50% are 3.68%, 4.78%, 0.25% and 5.35%, respectively, indicating that there is no obvious difference for the EDMs of specimens under the two model boundaries.

Figure 6c shows that in terms of CS, for the CJBs with $\beta = 60^\circ$ when the lateral pressure = 4 MPa, from the perspective of joint distance ratio, if the model boundaries are Case between plane stress and plane strain, the model CS rises in the beginning, but reduces as the joint distance ratio increases, in which the ratio of the highest value to the

lowest value of CS is 1.233. If the model boundaries are in plane strain, as the joint distance ratio rises, the model CS also increases firstly but decreases later. For this case, the ratio of the highest value to the lowest value of CS is 1.320. From the perspective of model boundary condition, the CS in Case II is higher than that in Case I. If the model boundaries vary from Case I to Case II, the increasing rates of CSs of specimens with joint distance ratios of 0%, 20%, 40% and 50% are 21.16%, 29.68%, 29.70% and 36.09%, respectively.

Figure 6d shows that for the CJBs with $\beta = 60^\circ$ when the lateral pressure = 4 MPa, if the model boundaries are Case II, the EDM of specimen displays a decreasing and increasing fluctuation trend with the growth of joint distance ratio. If the model boundaries are Case I, the model EDM reduces with the increase in joint distance ratio. From the perspective of model boundary condition, if the model boundaries vary from Case I to Case II, the increasing rates of EDMs of specimens with joint distance ratios of 0%, 20%, 40% and 50% are 9.32%, 13.46%, 11.17% and 11.78%, respectively.

Figure 7a,b displays the loading curves influenced by various joint distance ratios in the cases of two kinds of model boundaries. Figure 7a shows that for the CJBs with $\beta = 30^\circ$ when the lateral pressure of 4 MPa, if the model boundaries are Case I, the loading curves of specimens with various joint distance ratios will be closer. For Case II, the loading curves of specimens with different joint distance ratio show relatively obvious difference in the residual strength stage. Significantly, no residual strength stage exists on the loading curve for the joint distance ratio 0%, indicating that the macro instability of the model occurs. Regarding the perspective of model boundary condition, compared with Case I, the stress peak and residual strength of the model boundary condition in the case II are higher. As shown in Figure 7b, for the CJBs with $\beta = 60^\circ$ if the model boundaries are Case I, the loading curves influenced by various joint distance ratios show certain ductile failure characteristics, which is caused by the relatively strong confining pressure. For Case II, the loading curve for joint distance ratio 0% is with ductile failure characteristic, while the stress-strain curves for joint distance ratios 20%, 40% and 50% show brittle failure characteristics, which results from the obvious influence of confining pressure on CJB anisotropy. From the perspective of model boundary condition, compared with Case I, the stress peaks for Case II are higher.

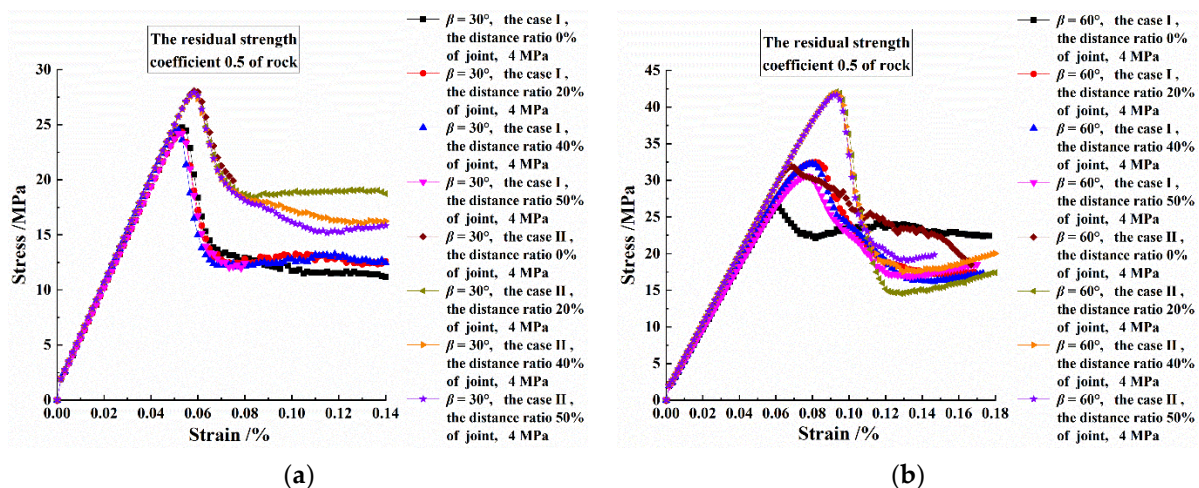


Figure 7. For the two kinds of model boundaries and the loading curves affected by various joint distance ratios: (a) for $\beta = 30^\circ$; (b) for $\beta = 60^\circ$ (Case I corresponding to the case between plane stress and plane strain and Case II corresponding to the plane strain).

3.2. Fracture Processes and Energy Evolutions under Different Joint Distance Ratios

3.2.1. Failure Modes under Different Column Dip Angles

Figure 8 displays the z-direction displacement contours of the CJBs with the joint distance ratios 0%, 50% and various β s under plane strain when the lateral pressure = 4 MPa. Figure 8a,h shows that for the CJBs with $\beta = 0^\circ$ and the joint distance ratio 0%, the columnar

joints in the upper zone of the mode are damaged, and there is a fluctuating strip fracture zone near the top of the model. Meanwhile, the sedimentation inside the model is distributed along the strip fracture zone. When the joint distance ratio is 50%, the fracturing of the columnar joints in the middle of the upper area of the model develops deeper and deeper. As presented in Figure 8b,i, for the CJBs with $\beta = 15^\circ$ and the joint distance ratio 0%, the columnar joints at the upper area of the model slide and become cracked due to the compression shear. Simultaneously, the sedimentation inside the model mainly develops along the dip angle of the cracked columns. For the condition of the joint distance ratio 50%, the joints within the upper area of the model slide and become damaged. As depicted in Figure 8c,j, for the CJBs with $\beta = 30^\circ$ and the joint distance ratio 0%, the columnar joints within the model slide under compression and shear, and the sedimentation at the right side of the upper part of the specimen is transmitted to deeper part. When the joint distance ratio is 50%, the joint slip characteristics and sedimentation inside the model are also basically same as the case of the joint distance ratio 0%. As shown in Figure 8d,k, for the CJBs with $\beta = 45^\circ$ and the joint distance ratio 0%, a relatively straight oblique shear zone appears within the model, which connects the upper left area as well as the lower right area of the specimen. For the condition of the joint distance ratio 50%, the oblique fracture zone inside the specimen is relatively curved, while the sedimentation still mainly developed following the oblique fractured area.

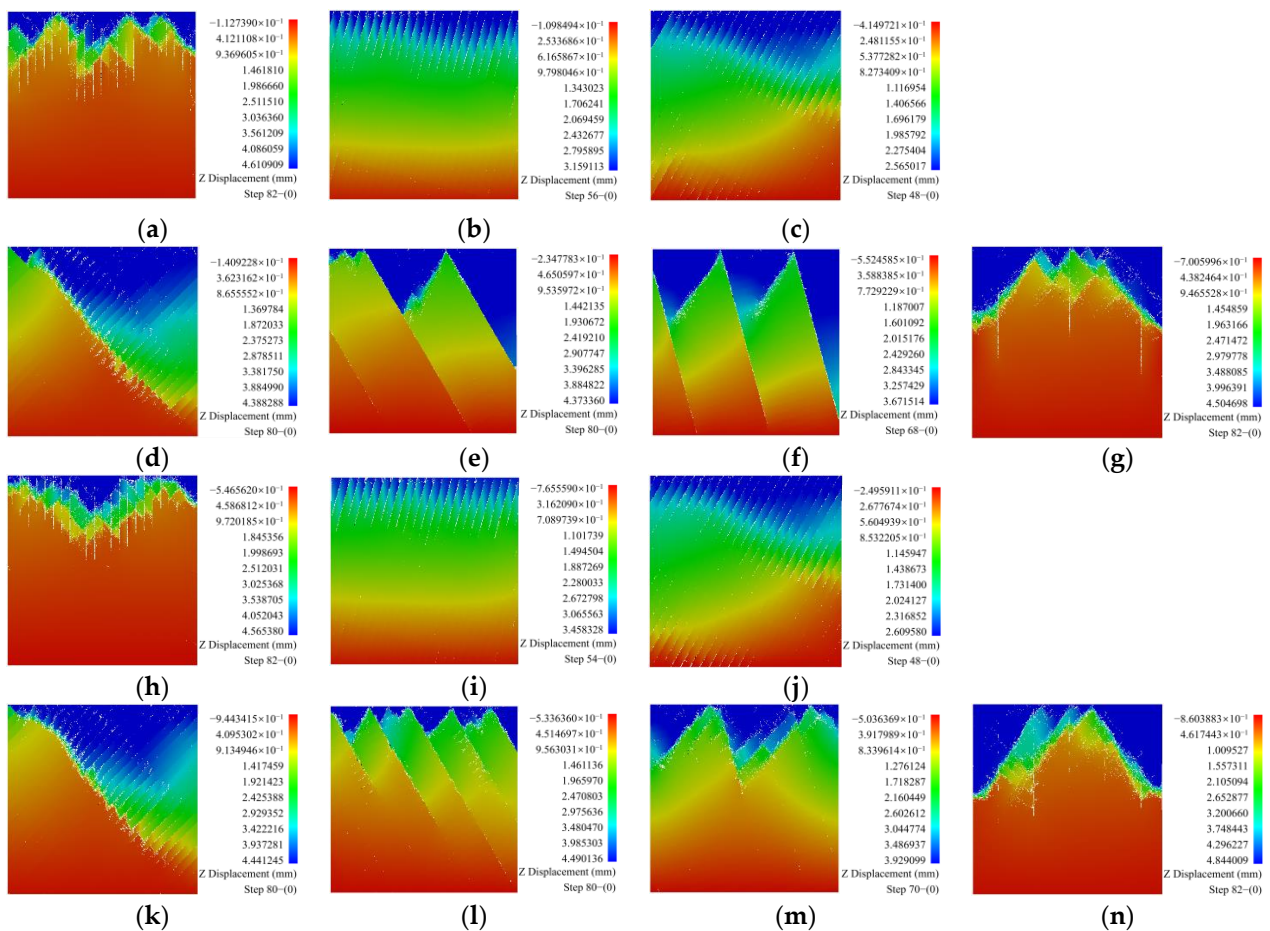


Figure 8. (a–g) The z-direction displacement diagrams of the CJBs with the joint distance ratio 0% and different column dip angles; (h–n) the z-direction displacement diagrams of the CJBs with the joint distance ratio 50% and different column dip angles.

As presented in Figure 8e,l, for the CJBs with $\beta = 60^\circ$ and the joint distance ratio 0%, the shear sliding occurs at the secondary joint set within the model. Additionally, the

shear fracture zone exists between the secondary joints in the upper area of the model. The sedimentation is basically distributed within the middle area and the right area of the upper part of the model, along the secondary joint set and shear fracture zone. When the joint distance ratio is 50%, the secondary joint sets at the upper middle part of the model are cut through, and the oblique shear fracture zones appear close to the upper end of the specimen. As depicted in Figure 8f,m, for the CJBs with $\beta = 75^\circ$ and the joint distance ratio 0%, the shear sliding at the secondary joint sets inside the specimen is relatively obvious. Additionally, there are two oblique shear fracture zones between the secondary joints at the upper zone of the model. The sedimentation is mainly distributed along the fracture zones and secondary joint sets, and in the right zone of the model, the sedimentation develops deeper and deeper. For the joint distance ratio = 50%, the shear sliding at the secondary joint sets is less obvious, and there are the oblique shear fracture zones at the upper part of the specimen. As shown in Figure 8g,n, for the CJBs with $\beta = 90^\circ$ and the joint distance ratio 0%, the secondary joint sets at the upper-middle area of the model are damaged, where an M-shaped shear fracture zone appears. The sedimentation mainly develops along the M-shaped shear fractured area. Namely, at the upper part of the model, the sedimentation is transmitted to a deeper depth. When the joint distance ratio is 50%, the secondary joint sets at the upper middle part of the model are also damaged. The M-shaped shear fracture zone and sedimentation distribution characteristics at the upper middle part of the model are also similar as the case of the joint distance ratio 0%.

3.2.2. Fracture Processes and Energy Evolutions under Different Column Dip Angles

(1) For the CJBs with $\beta = 30^\circ$ and the joint distance ratio 0%

Figure 9a displays the schematic diagram of the CJBs model with $\beta = 30^\circ$ and the joint distance ratio 0%, under the lateral pressure = 4 MPa. The stress-strain curve and AE energy are presented in Figure 9b,c. Meanwhile, the minor principal stress contours at the Points A~F are depicted in Figure 9d~i, describing the phenomenon of compression shear, sliding, and cracking of joints, crack initiation, propagation and rupture. The red zones on the minor principal stress diagram reflects the high-stress concentrations.

Combined with Figure 9b,d~i, it can be indicated that at the Point, the corresponding columnar joints and secondary joint sets inside the specimen show stress concentration. At the Point B, the columnar joints at the upper area of the model slide and become cracked. At the upper middle area of the model, high-stress concentration occurs along the edges of some columns, initially forming strip-shaped stress concentrations. When the loading is reduced to the Point C, the fractures generate and develop along the edges of some columns, the stresses is concentrated at the crack tips, and a strip-shaped stress concentration is formed inside the specimen. If the loading reaches the Point D, the fractures propagate further, the concentration extent of the original strip stress decreases, and there are stress concentrations along the edges of some columns at the right middle side of the specimen. When the loading reaches the Point E, the cracks initiate at the secondary joint sets. If the loading reaches the Point F, fractures intensify inside those strip fracture zones above the secondary joint sets. Moreover, there are strip damage zones at the upper surface and middle parts of the model. These columnar joints slide and become cracked in the middle upper part of the specimen. The secondary joint sets in the upper zone and the lower part of the model get damaged, and the secondary joint set at the middle of the model fails.

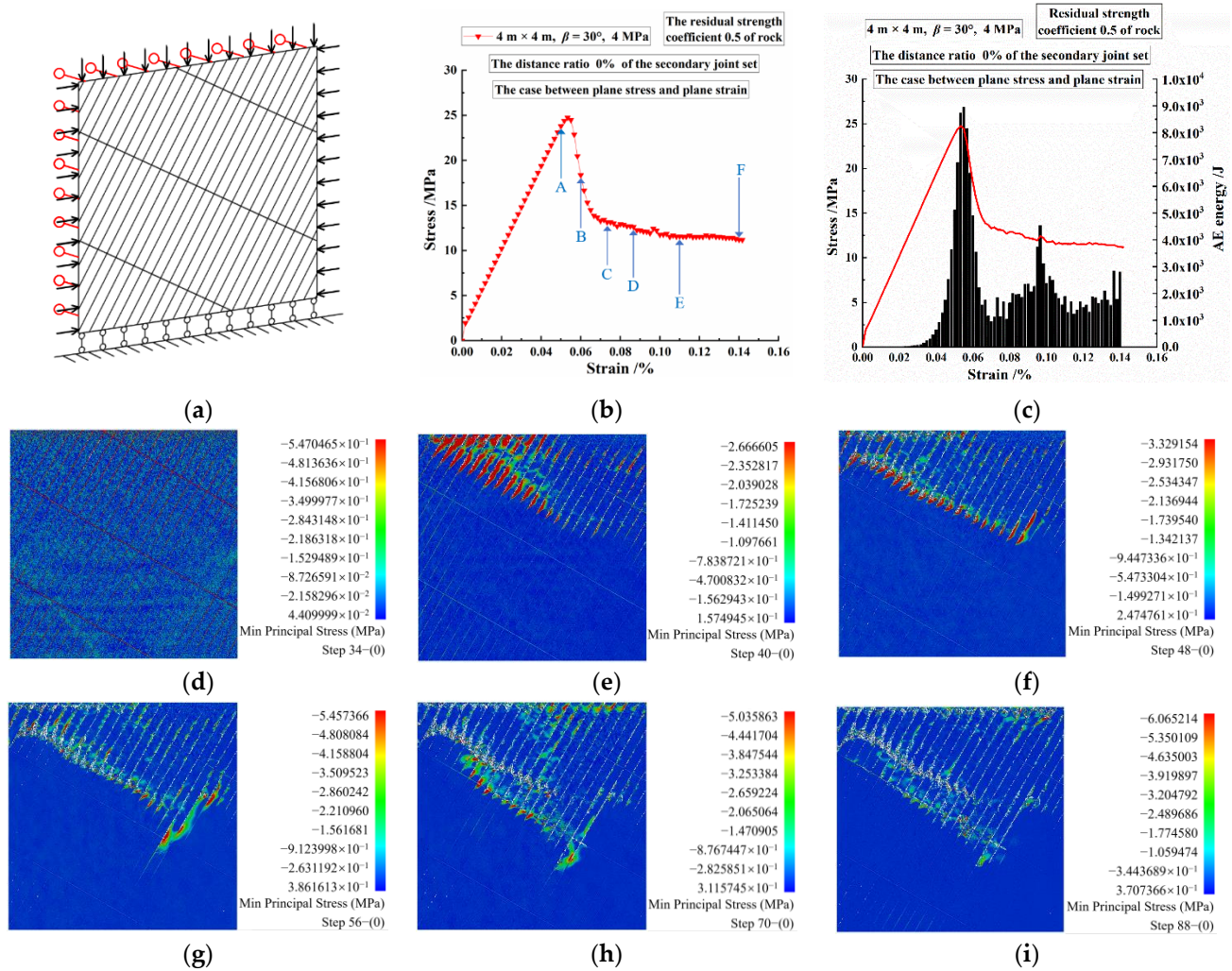


Figure 9. (a) For the case between plane stress and plane strain, the schematic diagram of the CJB model with $\beta = 30^\circ$ and the joint distance ratio 0%; (b,c) the loading curve and AE energy; (d–i) the minor principal stress contours at the Points A~F.

Figure 9c indicates that the AE energy release of the model shows roughly with the double-peak distribution. The 1st peak may be mainly caused by the damage-slip cracking at the upper middle area of the model. Meanwhile, the 2nd AE energy peak is mainly caused by the damage sliding at columnar joints at the middle area of the model and the crack creation and develop along the secondary joints.

(2) For the CJBs with $\beta = 30^\circ$ and the joint distance ratio 50%

Figure 10a shows the schematic diagram of the CJBs model with $\beta = 30^\circ$ and the joint distance ratio 50% when the lateral pressure = 4 MPa. Figure 10b,c displays the loading curve and AE energy. Figure 10d–i shows the minor principal stress contours at the Points A~F. Combined with Figure 10b,d–i, at the Point A, these joint sets and secondary joint sets inside the model show high-stress concentration. If the loading reaches Point B, the trend of compressive shear sliding along the columnar joint sets near the top of the specimen. If the loading reaches the Point C, the joint sets in the upper zone of the sample slide and become cracked, and several columns at the top of the model show stress concentrations. If the loading continues to decrease to the Point D, along the secondary joint set in the upper part of that specimen, cracks initiate and the stresses concentrate, forming a strip stress concentration zone. Near the upper end of the model, the columns also show stress concentration, forming another strip stress concentration zone. If the loading is reduced to the Point E, the stress concentrations are transferred to the vicinity below the position of

the secondary joint set. When the stress reaches Point F, in the upper zone of the sample and near the lower position of these secondary joint set, cracks are created and propagate, and the stresses are concentrated at the crack tips. Simultaneously, within the right middle part of the specimen, those joints slide under compression and shear, and the high-stress concentrations appear at the edge of the nearby column. Moreover, there are strip damage and fracture zones in the upper middle area of the model. In this area, the columnar joints are damaged, slide and become cracked. At the position of secondary joint set in the upper area of the model, the damage occurs. As shown in Figure 10c, the AE release of the model shows a single-peak distribution. The peak is as a result of the damaging, sliding and cracking of the columnar joints in the upper area of the sample.

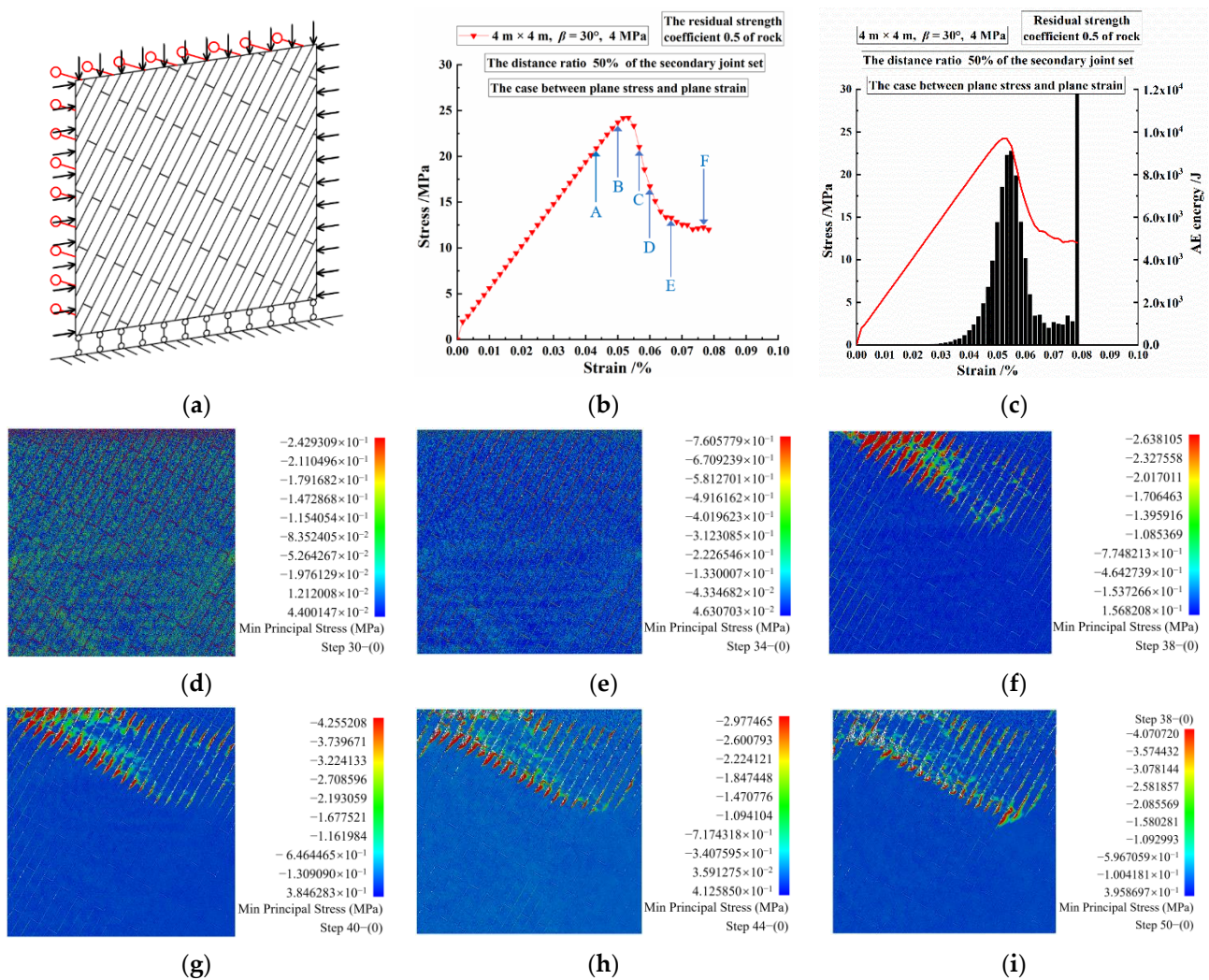


Figure 10. (a) For the case between plane stress and plane strain, the schematic diagram of the CJBs model with $\beta = 30^\circ$ and the joint distance ratio 50%; (b,c) the loading curve and AE energy; (d–i) the minor principal stress contours at the Points A~F.

(3) For the CJBs with $\beta = 75^\circ$ and the joint distance ratio 50%

Figure 11a displays the schematic diagram of the CJBs model with $\beta = 75^\circ$ and the joint distance ratio 50% under the lateral pressure = 4 MPa. The stress-strain curve and AE release are presented (see Figure 11b,c). The minor principal stress contours at the Points A~F are depicted in Figure 11d–i. Combined with Figure 11b,d–i, at the Point, the joints within the model and the secondary joint set at the middle of the model shows high-stress concentration. If the loading reaches the Point B, the secondary joints at the upper middle area of the model are damaged. In the meantime, the columns near it display obvious

stress concentration. If the loading drops to the Point C, crack initiation, propagation and penetration occur near the secondary joint set at the upper middle part of the model. In addition, there is an oblique shear fracture zone between the secondary joint sets. If the loading continues to decrease to the Point D, near the middle of the model, crack initiation, propagation and penetration at the secondary joints develop towards the lower area of the model. Simultaneously, crack creation and stress concentration happen near the secondary joints at the right side of the model. If the loading is reduced to the Point E, fractures along the secondary joint set of the specimen are intensified. Moreover, in the right middle part of the specimen, the shear fracture zones develop and the stresses at the tips of cracks are concentrated. If the loading reaches the Point F, the crushing inside the specimen will intensify.

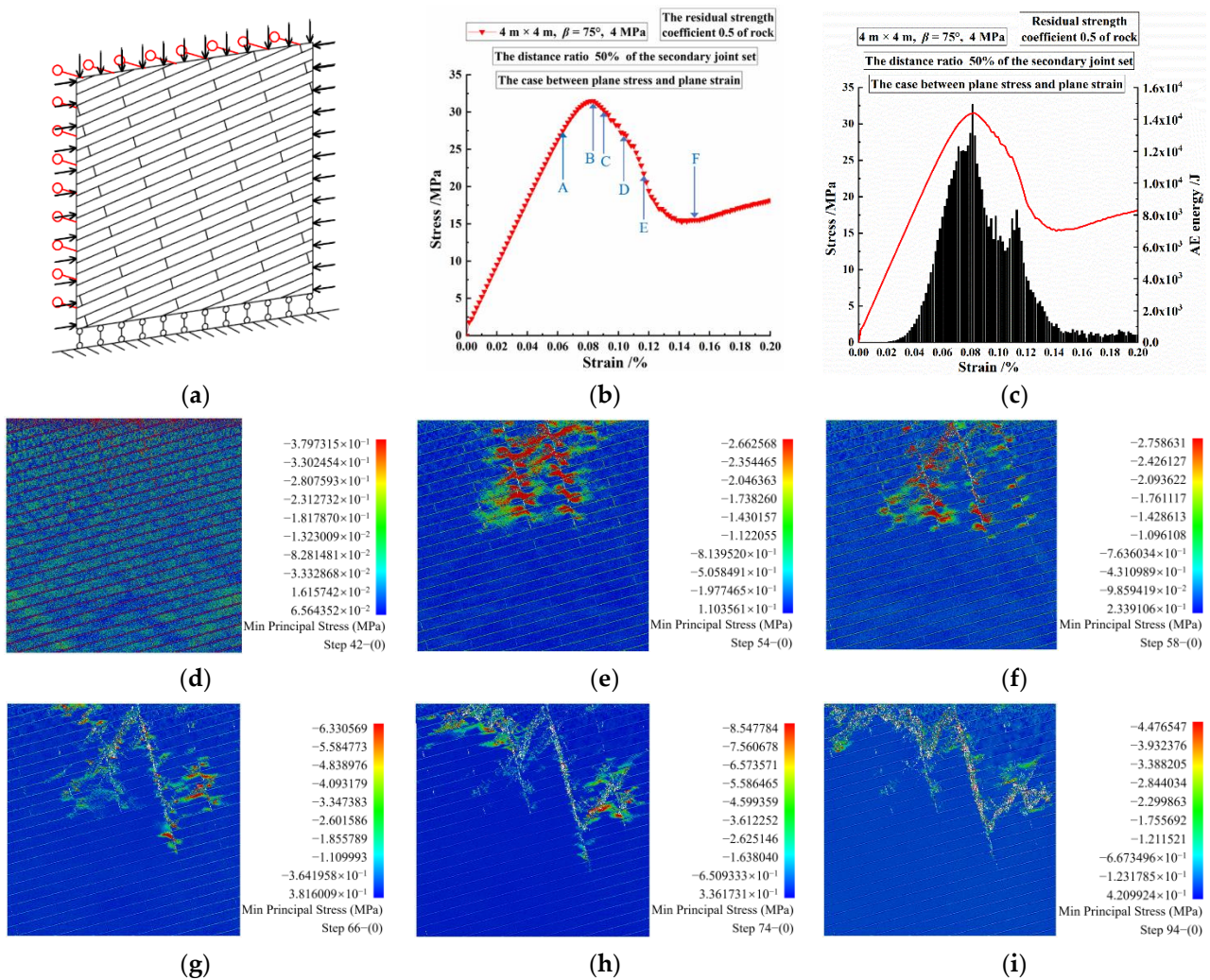


Figure 11. (a) For the case between plane stress and plane strain, the schematic diagram of the CJBs model with $\beta = 75^\circ$ and the joint distance ratio 50%; (b,c) the loading curve and AE energy; (d–i) the minor principal stress contours at the Points A~F.

Meanwhile, the joints within the model are damaged. The secondary joints at the upper area of the model are damaged and cracked, especially at the middle of the upper area of the model, where the damage and fracture penetrate. Close to the upper end of the model and at the right middle part of the model, the damaged zones are developed.

As displayed in Figure 11c, it is clear that the AE energy of the model displays the double-peak distribution. The first energy peak might be induced by the primary joint damage and the cracking of secondary joint set in the upper middle area of the model. The

second peak might be as a result of the fracture of the primary joints near the upper left area of the model and the development of the shear fracture zone in the right middle part of the model.

3.2.3. Fracture Processes and Energy Evolutions under Various Joint Distance Ratios and Column Dip Angle of 60°

(1) When the joint distance ratio = 0%

Figure 12a shows the schematic diagram of the CJBs model with $\beta = 60^\circ$ and the joint distance ratio 0% under the lateral pressure = 4 MPa. Figure 12b,c displays the loading curve and AE energy. Figure 12d–I shows the minor principal stress contours at the Points A~F. Combined with Figure 12b,d–i, at the Point A, the secondary joint set within the specimen shows high-stress concentrations, with the trend of compression shear sliding. If the loading goes to the Point B, the secondary joint sets inside the specimen gradually slide, and the high stress concentrations appear near the upper end of the specimen. If the loading reaches the Point C, the cracks are created near the upper end of the specimen. If the loading continues to decrease to the Point D, near the upper end of the model, the cracks propagate, and the stresses at the crack tips are concentrated. If the loading is reduced to the Point E, the cracks further develop in the upper area of the specimen, but the stress concentration reduces. If the loading reaches the Point F, fractures intensify from the secondary joints and fracture zones. At the middle of the right side of the specimen, the cracks initiate, and the stresses are concentrated. Meanwhile, the secondary joint sets slide, are damaged, compressed, and sheared. The damage fracture zones are developed near the top and at the upper area of the specimen.

Figure 12c shows that the AE energy of the specimen is roughly with four-peak distribution (or multi-peak distribution). The first energy peak might be as a result of the compression shear sliding at the secondary joint sets inside the specimen. The second peak might be mainly caused by the damage development of fractured zone near the top of the specimen. The third peak might be mainly as a result of the development of the fracture zone near the upper end of the model, the fracture zone in the upper zone of the model and the damage near the secondary joint sets. The fourth peak might be induced by the fracturing aggravation at the secondary joint sets and the initiation and propagation of cracks in the right middle area of the specimen.

(2) When the joint distance ratio = 20%

Figure 13a displays the schematic diagram of the CJBs model with $\beta = 60^\circ$ and the joint distance ratio 20% under the lateral pressure = 4 MPa. The loading curve and AE energy are shown in Figure 13b,c. The minor principal stress contours at the Points A~F are displayed in Figure 13d–i. Combined with Figure 13b,d–i, at the Point A, the secondary joint sets within the specimen show high-stress concentration. If the loading reaches the Point B, near the upper end of the specimen, the high-stress concentrations appear around the secondary joint sets. If the loading decreases to the Point C, the secondary joint sets get fractured at the upper area of the model. The stress concentration is obvious near the upper end of the model. When the loading continues to drop to the Point D, the creation and propagation of cracks occur within the original stress concentration areas. If the loading is reduced to the Point E, cracks further develop in the upper left and upper right parts of the model. When the loading reaches the Point F, the crushing in the upper zone of the model will intensify. Meanwhile, damage along columnar joint sets inside the specimen develops. The compressive shear fractures appear along the secondary joint sets. The damage fracture zones at the upper part of the model are formed. Figure 13c shows that the elastic energy of the specimen shows the single-peak distribution. The peak is induced by the compression-shear failure of the secondary joint sets, the damage of the primary joints and the columns in the upper part of the model.

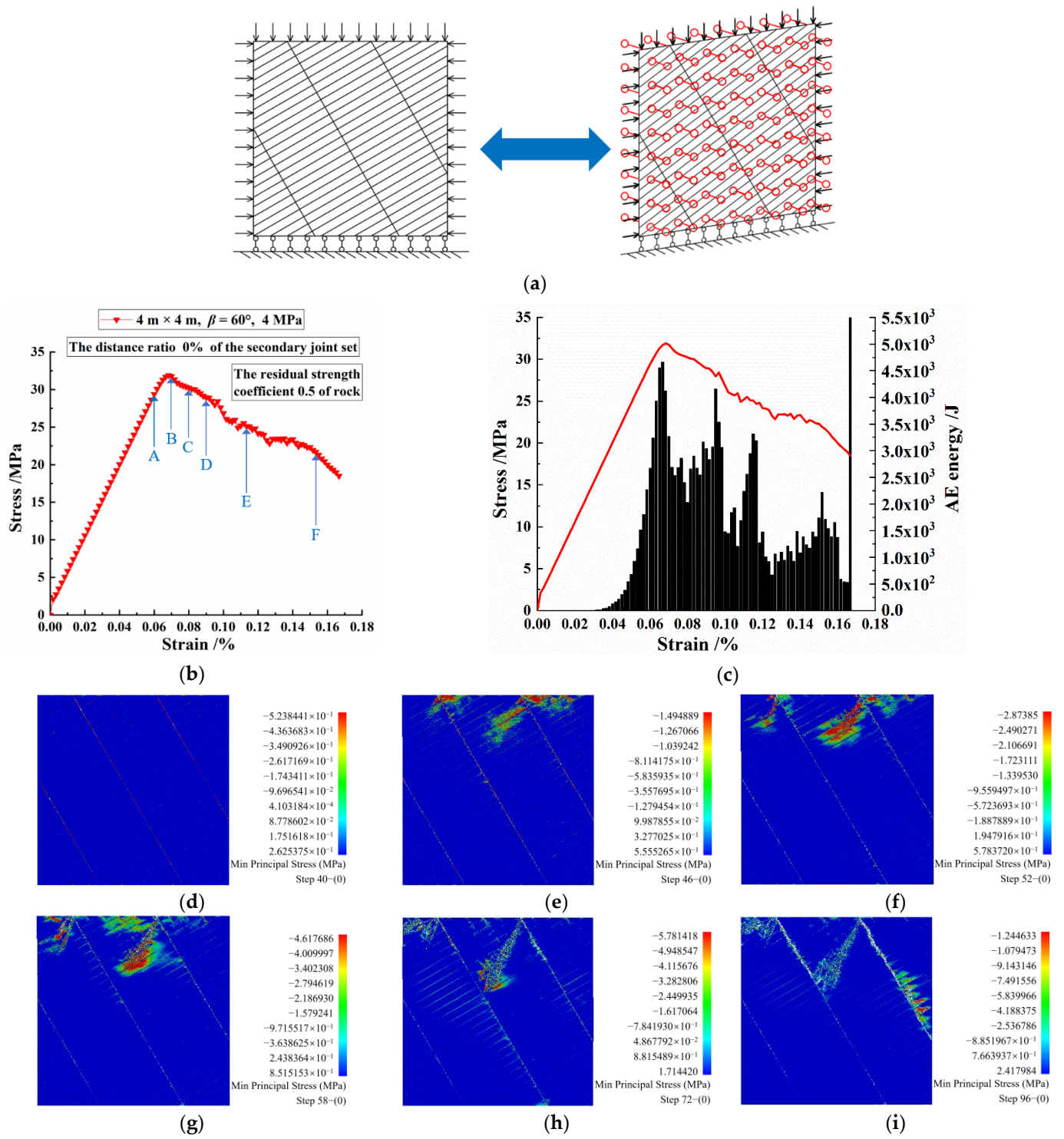


Figure 12. (a) Under plane strain, the schematic diagram of the CJBs model with $\beta = 60^\circ$ and the joint distance ratio 0%; (b,c) the loading curve and AE energy; (d~i) the minor principal stress contours at the Points A~F.

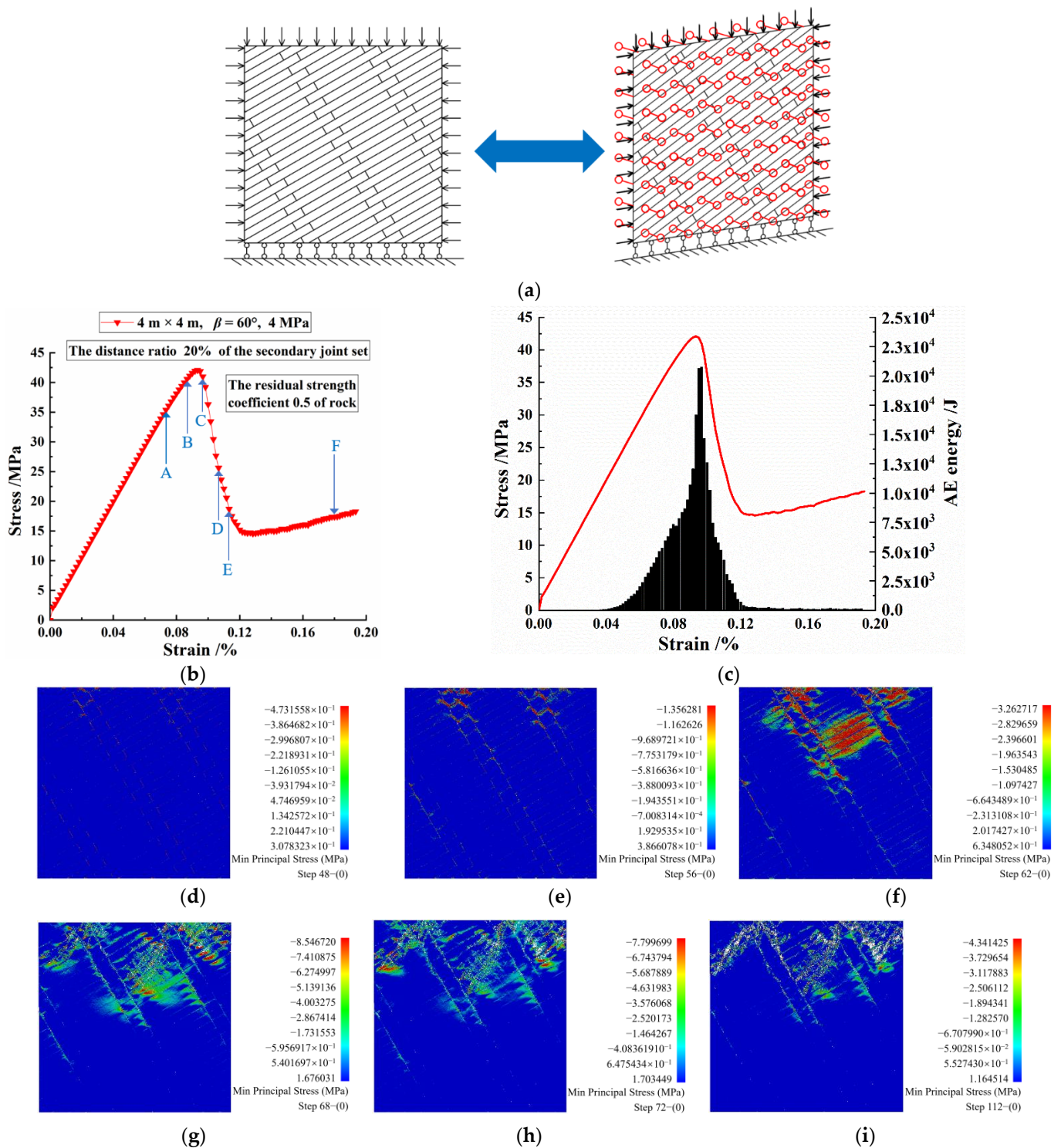


Figure 13. (a) Under plane strain, the schematic diagram of the CJBs model with $\beta = 60^\circ$ and the joint distance ratio 20%; (b,c) the loading curve and AE energy; (d–i) the minor principal stress contours at the Points A~F.

(3) When the joint distance ratio = 50%

Figure 14a shows the schematic diagram of the CJBs model with $\beta = 60^\circ$ and the joint distance ratio 50% under the lateral pressure = 4 MPa. Figure 14b,c displays the loading curve and AE energy. Figure 14d–i show the minor principal stress contours at the Points A~F. Combined with Figure 14b,d–i, at the Point A, the secondary joint sets within the

specimen are with a certain degree of stress concentration. If the loading reaches the Point B, the high stress concentrations are gradually significant near the secondary joint sets. If the loading is reduced to the Point C, the secondary joints slide, are compressed and sheared, and the creation and propagation of cracks and the high-stress concentration appears. If the loading decreases to the Point D, the compression shear and sliding at the secondary joint sets further develop. If the loading further decreases to the Point E, the compression shear and sliding fracture at the secondary joint sets develops towards the lower area of the model, but the extent of high-stress concentration reduces. If the loading is reduced to the Point F, the crushing intensifies near the top of the model and at the secondary joints. Meanwhile, there are the damage fracture zones developing towards the upper end of the model. The compression shear, damage and fracture appear at secondary joint sets. The damage at columnar joints is developed.

As presented in Figure 14c, the elastic energy of the model has a single-peak distribution. The peak is mainly as a result of the compression-shear damage and fracture of the secondary joint sets, as well as the failure of the columns near the upper end of the model.

(4) When the joint distance ratio = 50%

Figure 15a displays the schematic diagram of the CJBs model with $\beta = 60^\circ$ and the joint distance ratio 50%, in the case between plane stress and plane strain, under the lateral pressure = 4 MPa. The stress-strain curve and elastic energy are shown in Figure 15b,c. The minor principal stress contours at the Points A~F are depicted in Figure 15d-i. Combined with Figure 15b,d-i, at the Point A, the high-stress concentrations appear at the primary and secondary joints inside the model. If the loading is reduced to the Point B, the secondary joint sets get cracked in the upper zone of the model, and there will be obvious concentrated stresses around the secondary joint sets at the upper middle area of the model. When the loading decreases to the Point C, the cracks near the secondary joint sets initiate, propagate and penetrate in the upper area of the model, and the concentrated stresses move to the columns near the secondary joint sets. If the loading continues to decrease to the Point D, at the right side of the upper part of the specimen, the creation and propagation of cracks form along the columns around the secondary joints. If the loading reaches the Point E, the damage of the columns will intensify in the top zone of the specimen. Meanwhile, the damage of columnar joints inside the model develops. The secondary joints near the top part of the model are damaged and broken. The damage fracture zones are formed at the columns between the secondary joint sets. As displayed in Figure 15c, the AE energy of the specimen shows roughly the double-peak distribution. The first peak might be caused by the compression damage of primary joints, and the cracking of the secondary joint sets and surrounding columns. The second peak is basically as a result of the crack initiation of the columns at the upper left area of the model, and the crack propagation of the columns at the right side of the model.

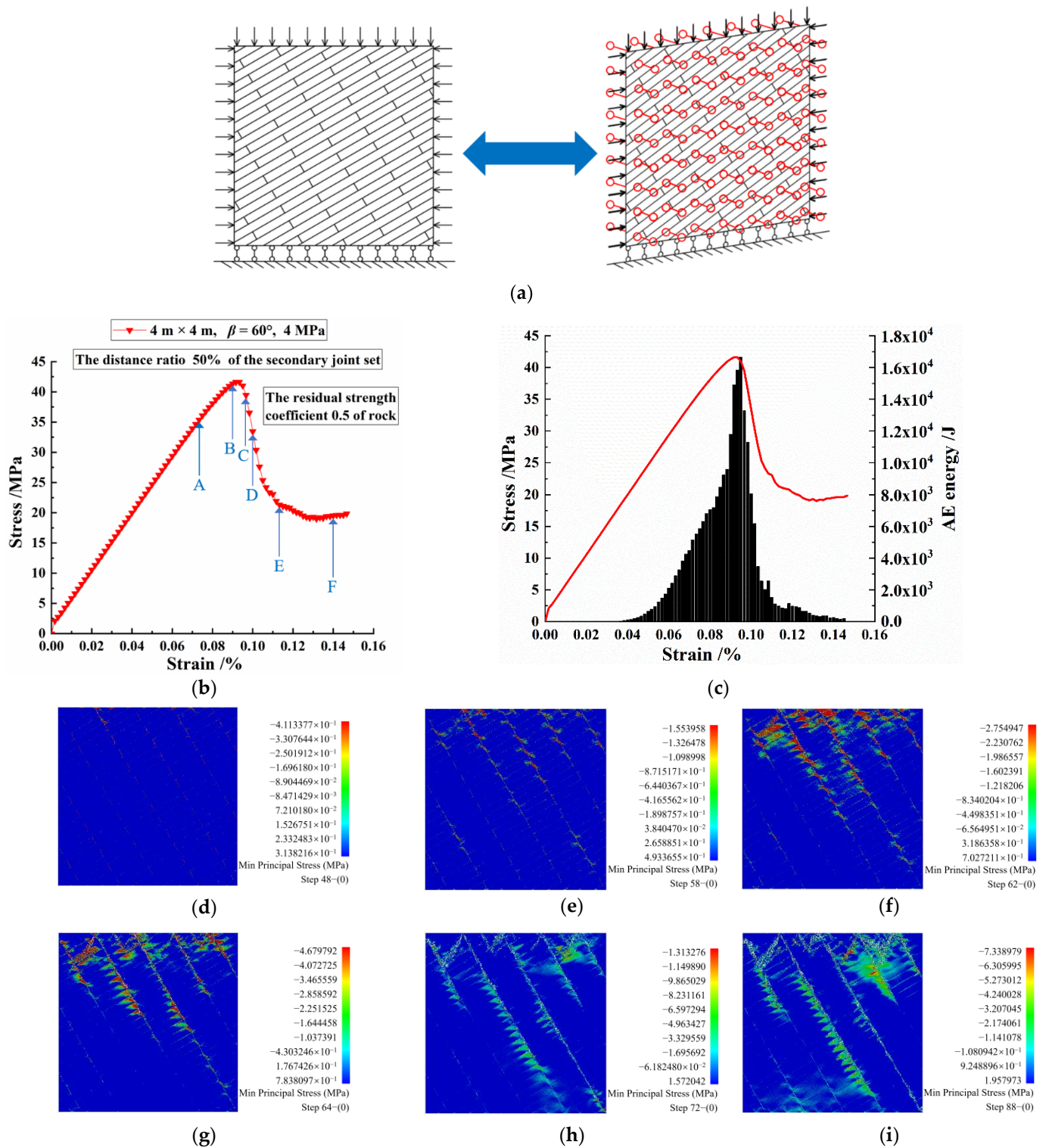


Figure 14. (a) Under plane strain, the schematic diagram of the CJBs model with $\beta = 60^\circ$ and the joint distance ratio 50%; (b,c) the loading curve and AE energy; (d–i) the minor principal stress contours at the Points A~F.

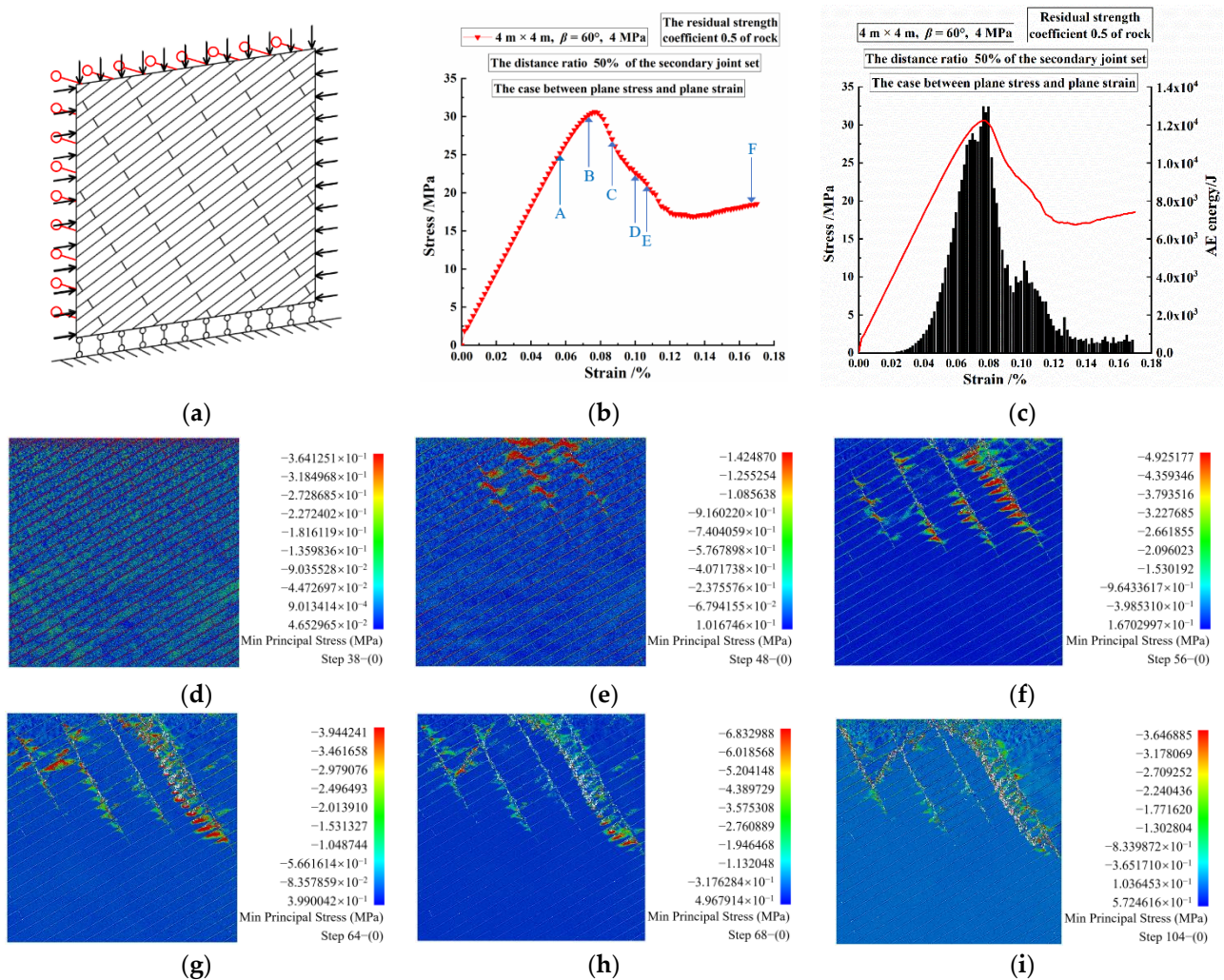


Figure 15. (a) For the case between plane stress and plane strain, the schematic diagram of the CJBs model with $\beta = 60^\circ$ and the joint distance ratio 50%; (b,c) the loading curve and AE energy; (d–i) the minor principal stress contours at the Points A~F.

3.3. The AE Counts and Energy Accumulations under Different Joint Distance Ratios

3.3.1. For the Case of Plane Strain

From Figure 16a–c, it is clear that for the CJBs with $\beta = 30^\circ$ and the joint distance ratio 0%, the AE count and energy accumulation change slightly in the beginning but increase sharply later. When the joint distance ratio is 20% and 50%, the variation trend of the AE count and energy accumulation is slow change, then shows a steep rise, and then slow growth. In terms of the accumulation magnitude of AE energy, the order from small to large is the joint distance ratios 0%, 20% and 50%, respectively. When the joint distance ratio is 0%, no residual strength stage exists on the loading curve, indicating that the overall instability of the model occurs. Before the instability failure, the AE count and energy accumulation are lower than those for the joint distance ratios 20% and 50%.

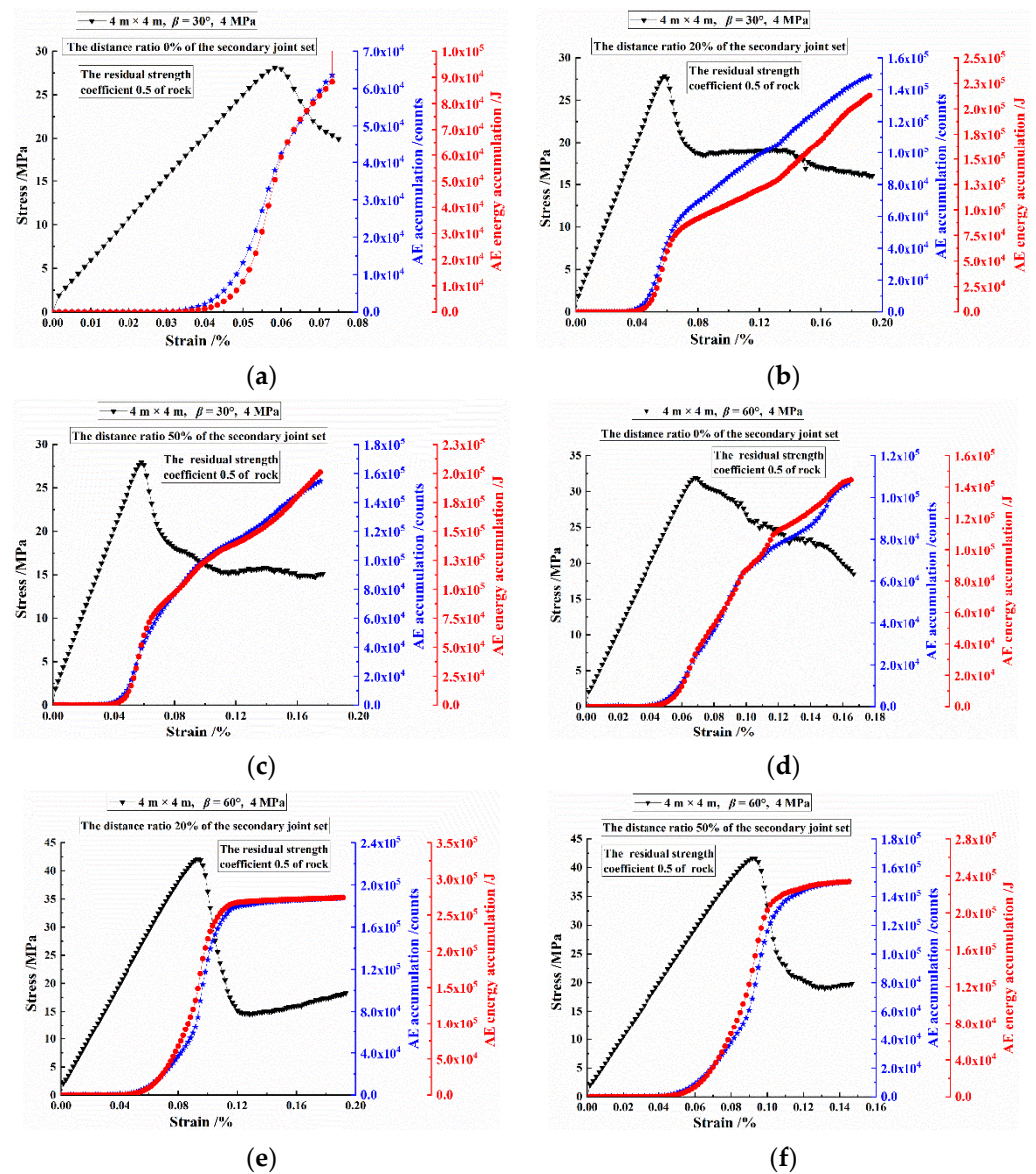


Figure 16. The AE counts and energy accumulations of the CJBs with different joint distance ratios: (a–c) for $\beta = 30^\circ$ and the joint distance ratios 0%, 20% and 50%, respectively; (d–f) for $\beta = 60^\circ$ and the joint distance ratios 0%, 20% and 50%, respectively.

As presented in Figure 16d–f, regarding the variation in the AE counts and energy accumulations, for the CJBs with $\beta = 60^\circ$ and the joint distance ratio 0%, the AE count and energy accumulation change gently at first and then grow. When the joint distance ratio is 20% and 50%, the variation trend of the AE count and energy accumulation is a slow change, then it increases, and then shows gentle variation. In terms of the accumulation magnitude of AE energy, the order from small to large is the joint distance ratios 0%, 50% and 20%, respectively. When the joint distance ratio is 20%, there is a higher degree of damage and fragmentation for the specimen under loading. Thus, the AE energy accumulations are higher than those for the joint distance ratios 0% and 50%.

3.3.2. For the Case between Plane Stress and Plane Strain

Figure 17 displays the AE counts and energy accumulations of the CJBs with various joint distance ratios. As depicted in Figure 17a–c, regarding the variation in the AE counts and energy accumulations, for the CJBs with $\beta = 30^\circ$ and the joint distance ratios 0%, 20% and 50%, the AE counts and energy accumulations firstly change slowly, then increase

sharply, and then grow gently. When the joint distance ratio is 50%, the residual strength stage of the loading curve is in short duration, the overall instability of the specimen occurs, so the gentle growth stages of the AE counts and energy accumulations are also short. In terms of the accumulation magnitude of AE energy, the order from small to large is the joint distance ratios 50%, 20% and 0%, respectively. For the joint distance ratio 0%, the model is seriously cracked and broken, so the AE counts and energy accumulations are higher than those for the joint distance ratios 50% and 20%.

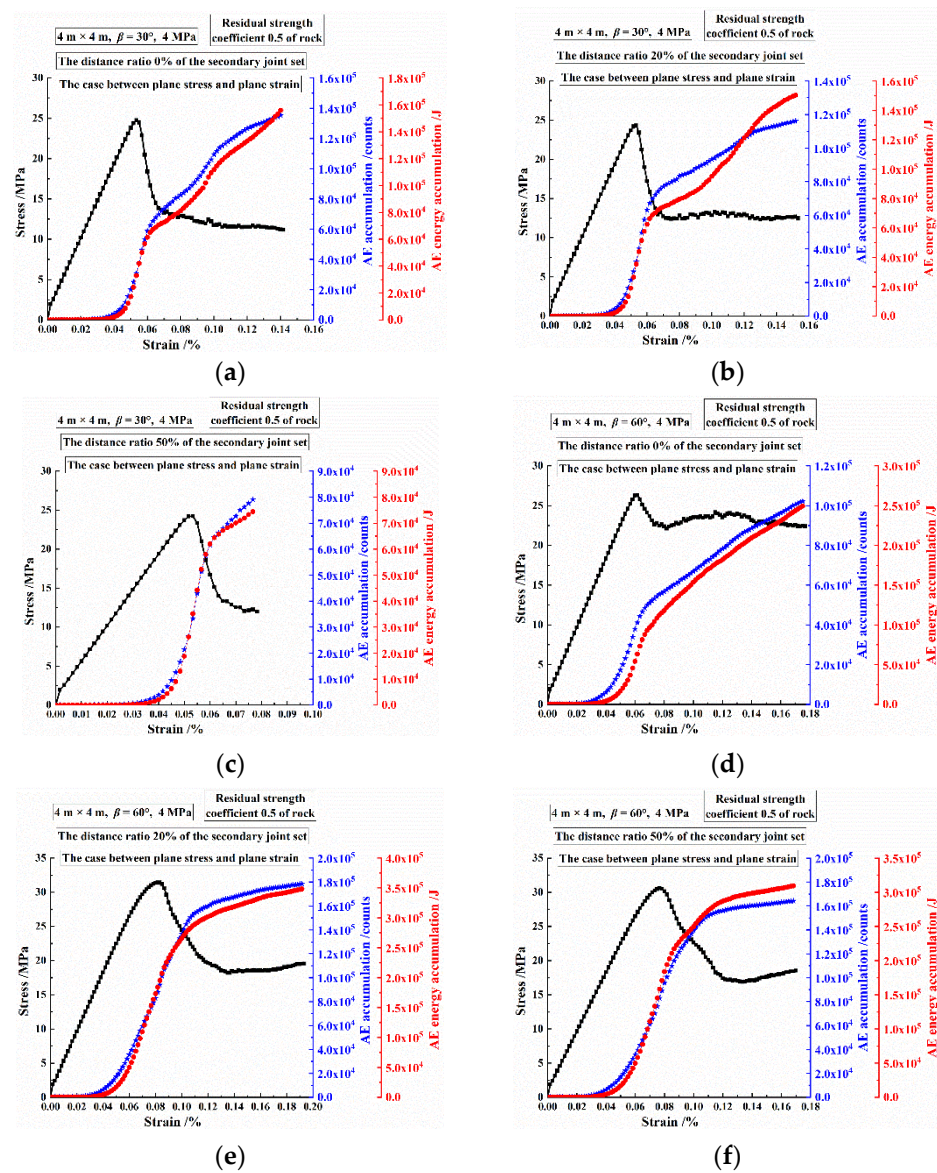


Figure 17. For the case between plane stress and plane strain, the AE counts and energy accumulations of the CJBs with different joint distance ratios: (a–c) for $\beta = 30^\circ$ and the joint distance ratios 0%, 20% and 50%, respectively; (d–f) for $\beta = 60^\circ$ and the joint distance ratios 0%, 20% and 50%, respectively.

As shown in Figure 17d–f, regarding the variation in the AE counts and energy accumulations, for the CJBs with $\beta = 60^\circ$ and the joint distance ratio 0%, they change slowly in the beginning, but then rise steeply, and grow gently later. When the joint distance ratio is 20% and 50%, the variation trend of the AE counts and energy accumulations is firstly slow change, then step increase and then gentle change. In terms of the accumulation magnitude of AE energy, the order from small to large is the joint distance ratios 0%, 50% and 20%, respectively. It can be inferred that for the CJBs with $\beta = 60^\circ$ and the joint distance

ratio 20%, there is a higher degree of fragmentation of the model, so the AE counts and energy accumulations are higher than those for the joint distance ratios 0% and 50%.

3.3.3. The AE Energy Accumulations under Compression

(1) For the case of plane strain

Figure 18 shows the accumulation of AE energy of the CJBs with various joint distance ratios, in the case of plane strain. As presented in Figure 18a, the accumulated AE energy corresponding to the stress peaks, occur in order of $\beta = 30^\circ, 45^\circ (60^\circ), 15^\circ, 75^\circ, 90^\circ$ and 0° , respectively. From the perspective of their magnitude from small to large, they are in order of $\beta = 75^\circ, 60^\circ, 15^\circ (30^\circ), 0^\circ, 90^\circ$ and 45° , respectively. As depicted in Figure 18b, the accumulated AE energy corresponding to the stress peaks occur in order of $\beta = 30^\circ, 45^\circ, 15^\circ, 60^\circ, 75^\circ$ and $0^\circ (90^\circ)$, respectively. From the perspective of their magnitude from small to large, they are in order of $\beta = 15^\circ, 30^\circ, 45^\circ, 90^\circ, 75^\circ, 0^\circ$ and 60° , respectively. According to Figure 18c, the accumulated AE energy corresponding to the stress peaks occur in order of $\beta = 30^\circ, 45^\circ, 15^\circ, 60^\circ, 75^\circ, 0^\circ$ and 90° , respectively. From the perspective of their magnitude from small to large, they are in order of $\beta = 15^\circ, 30^\circ, 90^\circ (0^\circ), 75^\circ, 45^\circ$ and 60° , respectively. As displayed in Figure 18d, the accumulated AE energy corresponding to the stress peaks occur in order of $\beta = 30^\circ, 45^\circ, 15^\circ, 60^\circ, 75^\circ, 90^\circ$ and 0° , respectively. From the perspective of their magnitude from small to large, they are in order of $\beta = 15^\circ, 90^\circ, 30^\circ, 75^\circ, 0^\circ, 45^\circ$ and 60° , respectively.

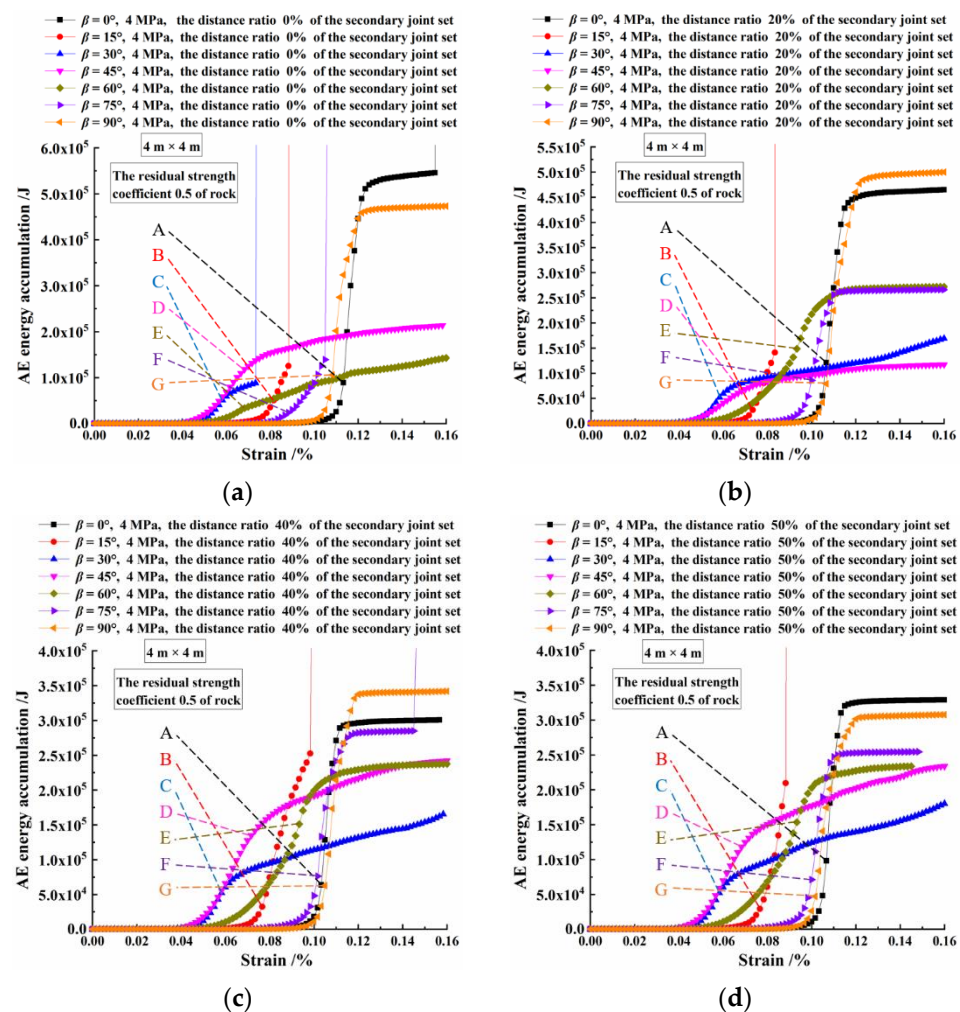


Figure 18. The AE energy accumulations for the peak stresses of the CJBs with different joint distance ratios: (a–d) for the joint distance ratios 0%, 20%, 40% and 50%.

(2) For the case of two kinds of model boundaries

Figure 19 displays the accumulated AE energy corresponding to the stress peaks of the CJBs with various joint distance ratios, in the case of two kinds of model boundaries. Case I is the case between plane stress and plane strain; Case II is the case of plane strain. As depicted in Figure 19a, regarding the CJBs with $\beta = 30^\circ$ when the lateral pressure = 4 MPa under Case I, the accumulated AE energy corresponding to the stress peaks fluctuates with the increase in joint distance ratio, in which the ratio of the highest value to the lowest is 1.284. However, for Case II, the accumulated AE energy corresponding to the stress peaks firstly grows gently, and then changes slowly as the joint distance ratio increases, in which the ratio of the highest value to the lowest is 1.034. Furthermore, the accumulated AE energy corresponding to the stress peaks in Case II is higher than Case I. If the model boundaries vary from Case I to Case II, for the joint distance ratios 0%, 20%, 40% and 50%, the accumulated AE energy corresponding to the stress peaks grow by 53.18%, 46.53%, 89.92% and 48.35%, respectively.

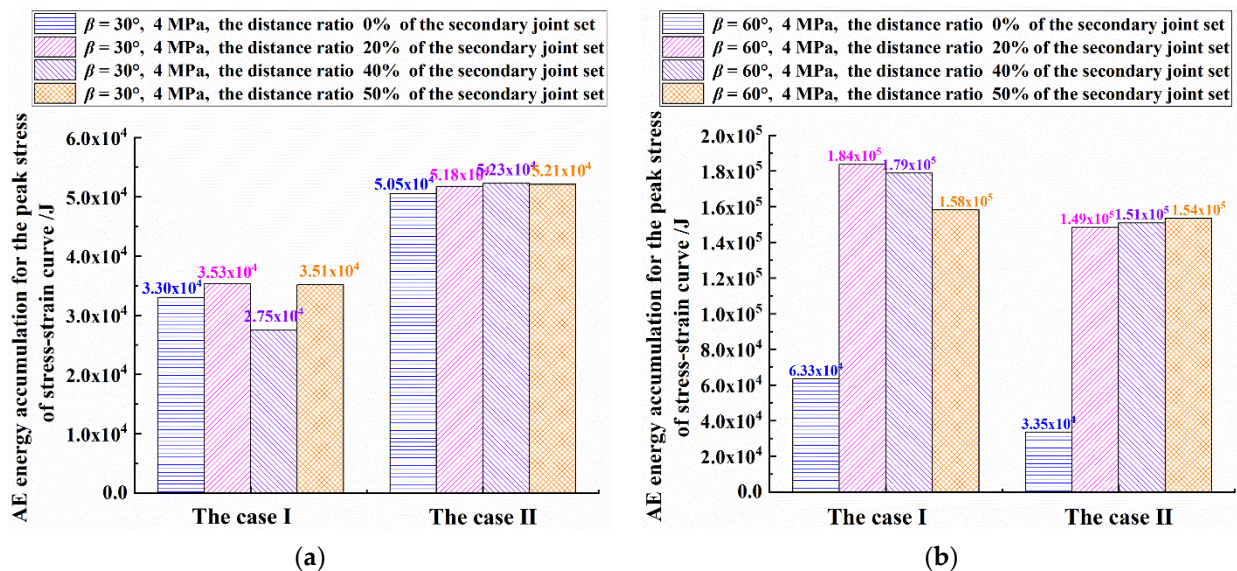


Figure 19. For the case of two kinds of model boundaries, for the CJBs with different joint distance ratios: (a) the accumulated AE energy corresponding to the stress peaks, for $\beta = 30^\circ$; (b) the AE energy accumulations corresponding to the peak stresses, for $\beta = 60^\circ$.

Figure 19b shows that when $\beta = 60^\circ$ and the lateral pressure = 4 MPa under Case I, the AE energy accumulation corresponding to the stress peaks increases sharply but reduces with the growth of joint distance ratio later, in which the ratio of the highest value to the lowest is 2.905, indicating the large variation range. For Case II, the accumulated AE energy corresponding to the stress peaks rises steeply and then grows slowly as the joint distance ratio rises, in which the ratio of the highest value to the lowest is 4.587, implying the great variation range. In addition, the accumulated AE energy corresponding to the stress peaks in Case II is lower than those in Case I. If the model boundaries vary from Case I to Case II, for the joint distance ratios 0%, 20%, 40% and 50%, the AE energy accumulations corresponding to the peak stresses increase by -47.15% , -19.23% , -15.53% and -2.98% , respectively.

4. Discussion

4.1. Influence of Joint Characteristics on CS and EDM

In the case of plane strain, under various joint distance ratios, the troughs of CS appear at $\beta = 30^\circ, 150^\circ, 210^\circ$ and 330° ; the peaks of CS appear at $\beta = 0^\circ, 90^\circ, 180^\circ$ and 270° . Additionally, for the CJBs with the joint distance ratios of 20%–50%, the CSs of specimens decrease sharply near $\beta = 0^\circ$ and 180° , but they change relatively gently near $\beta = 90^\circ$ and

270°. Under various joint distance ratios, the EDMs change in elliptical way as the column dip angle increases. The EDM of model is less sensitive to the variation in joint distance ratio. Moreover, the CS and EDM in Case II are higher than those in Case I.

Zheng et al. [31] performed shear tests on jointed granite samples. Their results showed that the shear strength peak grew with the normal stress or sawtooth angle increasing, but the shear stress-strain curves were not displayed to analyze further. Wang et al. [32] adopted the particle flow code (PFC) for studying the deforming and bearing properties of rock masses with varying joint density and argued that the specimen with a high joint density shows low strength. However, the jointed rock masses were with discrete fracture networks, and it was inconvenient for understanding anisotropy of jointed rock masses. Fan et al. [33] adopted the three-dimensional PFC to reproduce the physico-mechanical properties of multiple non-persistent joints subject to uniaxial loading, and analyzed the changing of CSs as the dip-angle and length of joints increase. Moreover, with the increase in joint length, the rock CS will be more and more sensitive to the change of the dip angle. Nevertheless, the influence of lateral pressures on the CS and EDM of rock mass specimens was not taken into account. Wu et al. [34] applied the numerical simulation method to calculate the anisotropy of strength and deformation of jointed rock masses. However, the distribution of joint dip angles, joint trace lengths and joint spacings are different from the specimens in this paper.

4.2. Influence of Joint Characteristics on Fracture Mechanism

Taking the following case in this paper for example: the CJBs models with $\beta = 60^\circ$ and the joint distance ratios 0% and 50% under plane strain. When the joint distance ratio is 0%, with the increase in loading, the secondary joint sets inside the specimen gradually slide under compression and shear, and the high-stress concentrations occur close to the upper end of the specimen. After that, the cracks initiate. As the loading grows, the cracks further develop in the upper zone of the model, but the stress concentration reduces. As the loading further increases, the fracture intensifies along the secondary joints and fractured zones. At the middle of the right side of the specimen, the cracks initiate and the stresses are concentrated.

When the joint distance ratio is 50%, with the growing of loading, the high-stress concentrations are gradually significant near the secondary joint sets. As the loading continues to rise, at the upper area of the model, the secondary joint sets slide, are compressed and sheared, the fractures are created and develop, and the concentrated stresses appear. With the increase in loading, the compression shear and sliding at the secondary joint sets further develop, and the fractures also generate and propagate near the upper end of the model. As the loading further increases, the compression shear and sliding fracture at the secondary joint sets develops towards the lower end of the model, but the extent of high-stress concentration reduces. With the loading further growing, the crushing intensifies towards the upper surface of the model and at the secondary joint sets.

Zhou et al. [35] used the two-dimensional PFC method to compute the physico-mechanical parameter values of specimens with single and double joints. However, the influence of lateral pressures on the failure mechanisms of specimens were not taken into account. Wu et al. [34] analyzed the cracking modes of jointed rocky masses subject to lateral pressure by using the numerical simulation method. Nevertheless, the dip angles, trace lengths and spacings of joints obey to the normal, lognormal and negative exponential distributions, respectively. As a result, the fracture features were different from the specimens in this study. Chen et al. [36] suggested that affected by varying lateral pressure, the loading curve of granite specimens containing pre-existing micro-cracks has the feature of stepped brittle drops. Fan et al. [33] discussed the fracture mechanisms and failure patterns of multiple non-persistent joints under uniaxial loading by using the PFC3D method, and analyzed the influence of the dip angles and lengths of joints on the fracture mechanisms. However, the lateral pressures were not taken into account.

4.3. Influence of Joint Characteristics on Acoustic Emission

Taking the following case in this paper for example: the CJBs models with $\beta = 60^\circ$ and the joint distance ratios 0% and 50% under plane strain. When the joint distance ratio is 0%, the AE energy released of the model shows roughly the distribution of four peaks. The first energy peak might result from the fracture and compression shear sliding at the secondary joint sets inside the specimen. The second energy peak might be caused by the damage development of the fracture zone at the upper part of the specimen. The third energy peak might result from the development of the fracture zone close to the upper end of the model, the development of the fracture zone in the top zone of the model and the damage near the secondary joint sets. The fourth energy peak might be caused by the crack aggravation at the secondary joint sets and the creation and propagation of cracks in the middle right zone of the model.

When the joint distance ratio is 50%, the released AE energy of the model shows the single peak distribution. The AE energy peak might mainly result from the compressive shear, damage and fracture of the secondary joint sets, as well as the damage of columns near the upper end of the model.

The tests conducted by Meng et al. [37] show that with the increase in normal stress, the initial slope of shear-stress vs. shear-strain curve of cement mortars increases, while the AE activity gradually lags on the strain axis. However, the stress or damage diagrams corresponding to the AE activities were not displayed to further investigate mechanical behaviors of the specimens. The tests obtained by Guo et al. [38] show that the smaller the joint continuity rate, the more lagging the AE activity for the rock bridge failure point on the time axis. This conclusion is similar with the order of AE energy accumulations in certain cases of this paper. For example, for the CJBs with $\beta=60^\circ$ or 75° , when the joint distance ratio grows from 0% to 50%, the AE energy accumulation at the peak stresses lags along the strain axis. By the combination of the laboratory physical test and numerical test, Zhang et al. [39] summarized the influences of normal stiffnesses and joint dip angles on the fracture mechanisms and AE energy accumulations of specimens with en-echelon joints. Nevertheless, there are certain differences for the AE energy accumulations due to geometric difference between the en-echelon joints and columnar joints. The tests by Wang et al. [40] show that the AE energy accumulation increases with the growth of joint roughness, which provides insights for future related work of CJBs in this study.

5. Conclusions

Based on the meso-damage mechanics and the statistical damage theory, a group of numerical nonuniform CJB samples with various dip angles of columns and distance ratios of secondary joints were established. The continuous fracture and AE release processes of CJBs were captured, and the AE-induced energy release rules were discussed. The conclusions can be drawn as follows:

Under plane strain, the troughs of CS appear at the column dip angles $\beta = 30^\circ, 150^\circ, 210^\circ$ and 330° ; the peaks of CS appear at $\beta = 0^\circ, 90^\circ, 180^\circ$ and 270° under different joint distance ratios. Meanwhile, for the CJBs with the joint distance ratios of 20%~50%, the CSs of specimens decrease sharply near $\beta = 0^\circ$ and 180° , but they change relatively gently near $\beta = 90^\circ$ and 270° . In terms of EDM, it changes in elliptical way with increasing column dip angle under different joint distance ratios. The EDM of specimen is less sensitive to the variation in joint distance ratio. Under plane strain, the CSs and EDMs are higher than the corresponding values in the case between plane stress and plane strain. These rules can provide the theoretical basis for determining in situ parameters, tunnel axis in transportation engineering, excavation direction in mining engineering and so on.

In the case between plane stress and plane strain, when $\beta = 30^\circ$ and the joint distance ratio = 0%, the columnar joints slide and are compressed; cracks occur near the upper end of the model as the loading grows. Especially, the high stresses will concentrate along the edges of the columns and result in the creation and propagation of cracks at the upper top part of the specimen. As the loading increases, the shear failure happens at the

middle part of the model because of high shear stresses. Simultaneously, many fractures develop at the secondary joint sets and the crushing intensifies within the strip fracture zone above the secondary sets. Under plane strain, when $\beta = 60^\circ$ and the joint distance ratio = 50%, the stress concentrations are gradually obvious near the secondary joint sets with the loading increasing. Then, these joints slide, are compressed and sheared. The high stress releases due to the newly formed cracks and rebuilds up at the tips of cracks, which leads the fracture of the secondary joints to developing towards the lower end of the model. However, the extent of stress concentration gradually reduces. With the gradual processes of stress concentration, stress release and stress transfer, the crushing intensifies near the top of the specimen and at the secondary joints. These results will contribute to the maintenance, support design and reinforcement of slopes and tunnels located at CJBs.

Under plane strain, when the joint distance ratio = 50%, the AE energy accumulations corresponding to the stress peaks occur along the strain axis in order of $\beta = 30^\circ, 45^\circ, 15^\circ, 60^\circ, 75^\circ, 90^\circ$ and 0° . In terms of the magnitude, they occur in the order from small to large when $\beta = 15^\circ, 90^\circ, 30^\circ, 75^\circ, 0^\circ, 45^\circ$ and 60° , successively. Moreover, when $\beta = 30^\circ$ under the lateral pressure, the accumulated AE energy corresponding to the stress peaks under plane strain is higher than those in the case between plane stress and plane strain. However, when β increases to 60° , the former ones become lower than the later ones, which implies the critical transformation of the influence of column dip angles on the AE energy-related fracture precursor. These achievements can help to promote the disaster prevention and mitigation for slope sliding, slope toppling and tunnel collapse which may cause severe damage by revealing the failure precursors of rock masses.

Author Contributions: Conceptualization, B.G.; data curation, Y.W.; formal analysis, Y.W.; funding acquisition, B.G. and C.T.; investigation, Y.W. and X.Y.; software, C.T.; supervision, B.G. and C.T.; writing—original draft, Y.W.; writing—review and editing, B.G., Y.Z. and X.Y. All authors have read and agreed to the published version of the manuscript.

Funding: This research was funded by the National Natural Science Foundation of China (Grant Nos. 41941018 and 42102314), the National Basic Research Program of China (Grant No. 2018YFC1505301), and the China Postdoctoral Science Foundation (Grant No. 2020M680950), for which the authors are grateful.

Data Availability Statement: The datasets generated and/or analyzed during the current study are available from the corresponding author upon reasonable request.

Conflicts of Interest: The authors declare no conflict of interest.

Symbol and Abbreviation

Symbol

σ	Stress
f_{c0}	Uniaxial compressive strength
f_{t0}	Uniaxial tensile strength
f_{cr}	Residual compressive strength
f_{tr}	Residual tensile strength
ε	Strain
ε_{c0}	Strain at f_{c0}
ε_{t0}	Strain at f_{t0}
ε_{tu}	Ultimate tensile strain

Abbreviation

CJRM	Columnar jointed rock mass
CJB	Columnar jointed basalt
CS	Compressive strength
EDM	Equivalent deformation modulus

References

1. Zheng, W.T.; Xu, W.Y.; Ning, Y.; Meng, G.T. Scale effect and anisotropy of deformation modulus of closely jointed basaltic mass. *J. Eng. Geol.* **2010**, *18*, 559–565.
2. Jiang, Q.; Feng, X.T.; Hatzor, Y.H.; Hao, X.J.; Li, S.J. Mechanical anisotropy of columnar jointed basalts: An example from the Baihetan hydropower station, China. *Eng. Geol.* **2014**, *175*, 35–45. [[CrossRef](#)]
3. Li, G.; Wang, K.; Gong, B.; Tao, Z.G.; Du, K. A multi-temporal series high-accuracy numerical manifold method for transient thermoelastic fracture problems. *Int. J. Solids Struct.* **2021**, *230*, 111151. [[CrossRef](#)]
4. Jin, C.Y.; Li, S.G.; Liu, J.P. Anisotropic mechanical behaviors of columnar jointed basalt under compression. *Bull. Eng. Geol. Environ.* **2018**, *77*, 317–330. [[CrossRef](#)]
5. Milazzo, M.P.; Keszthelyi, L.P.; Jaeger, W.L.; Rosiek, M.; Mattson, S.; Verba, C.; Beyer, R.A.; Geissler, P.E.; McEwen, A.S.; Hi, R.T. Discovery of columnar jointing on Mars. *Geology* **2009**, *37*, 171–174. [[CrossRef](#)]
6. Goehring, L.; Mahadevan, L.; Morris, S.W. Nonequilibrium scale selection mechanism for columnar jointing. *Proc. Natl. Acad. Sci. USA* **2009**, *106*, 387–392. [[CrossRef](#)] [[PubMed](#)]
7. Meng, Q.X.; Wang, H.L.; Xu, W.Y.; Chen, Y.L. Numerical homogenization study on the effects of columnar jointed structure on the mechanical properties of rock mass. *Int. J. Rock Mech. Min. Sci.* **2019**, *124*, 104127. [[CrossRef](#)]
8. Yan, L.; Xu, W.Y.; Wang, R.B.; Meng, Q.X. Numerical simulation of the anisotropic properties of a columnar jointed rock mass under triaxial compression. *Eng. Comput.* **2018**, *35*, 1788–1804. [[CrossRef](#)]
9. Niu, Z.H.; Zhu, Z.D.; Que, X.C. Constitutive model of stress-dependent seepage in columnar jointed rock mass. *Symmetry* **2020**, *12*, 160. [[CrossRef](#)]
10. Xiang, Z.P.; Wang, H.L.; Xu, W.Y.; Xie, W.C. Experimental study on hydro-mechanical behaviour of anisotropic columnar jointed rock-like specimens. *Rock Mech. Rock Eng.* **2020**, *53*, 5781–5794. [[CrossRef](#)]
11. Ke, Z.Q.; Wang, H.L.; Xu, W.Y.; Lin, Z.N.; Ji, H. Experimental study of mechanical behaviour of artificial columnar jointed rock mass containing transverse joints. *Rock Soil Mech.* **2019**, *40*, 660–667.
12. Shi, A.C.; Wei, Y.F.; Zhang, Y.H.; Tang, M.F. Study on the strength characteristics of columnar jointed basalt with a true triaxial apparatus at the Baihetan hydropower station. *Rock Mech. Rock Eng.* **2020**, *53*, 4947–4965. [[CrossRef](#)]
13. Ji, H.; Zhang, J.C.; Xu, W.Y.; Wang, R.B.; Wang, H.L.; Yan, L.; Lin, Z.N. Experimental investigation of the anisotropic mechanical properties of a columnar jointed rock mass: Observations from laboratory-based physical modelling. *Rock Mech. Rock Eng.* **2017**, *50*, 1919–1931. [[CrossRef](#)]
14. Que, X.C.; Zhu, Z.D.; Niu, Z.H.; Lu, W.N. Estimating the strength and deformation of columnar jointed rock mass based on physical model test. *Bull. Eng. Geol. Environ.* **2020**, *80*, 1557–1570. [[CrossRef](#)]
15. Feng, X.T.; Hao, X.J.; Jiang, Q.; Li, S.J.; Hudson, J.A. Rock cracking indices for improved tunnel support design: A case study for columnar jointed rock masses. *Rock Mech. Rock Eng.* **2016**, *49*, 2115–2130. [[CrossRef](#)]
16. Hao, X.J.; Feng, X.T.; Yang, C.X.; Jiang, Q.; Li, S.J. Analysis of EDZ development of columnar jointed rock mass in the Baihetan diversion tunnel. *Rock Mech. Rock Eng.* **2016**, *49*, 1289–1312. [[CrossRef](#)]
17. Chen, B.R.; Li, Q.P.; Feng, X.T.; Xiao, Y.X.; Feng, G.L.; Hu, L.X. Microseismic monitoring of columnar jointed basalt fracture activity: A trial at the Baihetan Hydropower Station, China. *J. Seismol.* **2014**, *18*, 773–793. [[CrossRef](#)]
18. Xiao, Y.X.; Feng, X.T.; Chen, B.R.; Feng, G.L.; Yao, Z.B.; Hu, L.X. Excavation-induced microseismicity in the columnar jointed basalt of an underground hydropower station. *Int. J. Rock Mech. Min. Sci.* **2017**, *97*, 99–109. [[CrossRef](#)]
19. Jiang, Q.; Wang, B.; Feng, X.T.; Fan, Q.X.; Wang, Z.L.; Pei, S.F.; Jiang, S. In situ failure investigation and time-dependent damage test for columnar jointed basalt at the Baihetan left dam foundation. *Bull. Eng. Geol. Environ.* **2019**, *78*, 3875–3890. [[CrossRef](#)]
20. Liang, Z.Z.; Gong, B.; Li, W. Instability analysis of a deep tunnel under triaxial loads using a three-dimensional numerical method with strength reduction method. *Tunn. Undergr. Space Technol.* **2019**, *86*, 51–62. [[CrossRef](#)]
21. Gong, B.; Wang, Y.Y.; Zhao, T.; Tang, C.A.; Yang, X.Y.; Chen, T.T. AE energy evolution during CJB fracture affected by rock heterogeneity and column irregularity under lateral pressure. *Geomat. Nat. Hazards Risk* **2022**, *13*, 877–907. [[CrossRef](#)]
22. Feng, X.H.; Gong, B.; Tang, C.A.; Zhao, T. Study on the non-linear deformation and failure characteristics of EPS concrete based on CT-scanned structure modelling and cloud computing. *Eng. Fract. Mech.* **2022**, *261*, 108214. [[CrossRef](#)]
23. Liang, Z.Z.; Gong, B.; Wu, X.K.; Zhang, Y.B.; Tang, C.A. Influence of principal stresses on failure behavior of underground openings. *Chin. J. Rock Mech. Eng.* **2015**, *34*, 3176–3187.
24. Gong, B.; Wang, S.Y.; Sloan, S.W.; Shen, D.C.; Tang, C.A. Modelling rock failure with a novel continuous to discontinuous method. *Rock Mech. Rock Eng.* **2019**, *52*, 3183–3195. [[CrossRef](#)]
25. Wang, Y.Y.; Gong, B.; Tang, C.A.; Zhao, T. Numerical study on size effect and anisotropy of columnar jointed basalts under uniaxial compression. *Bull. Eng. Geol. Environ.* **2022**, *81*, 41. [[CrossRef](#)]
26. Chen, B.P.; Gong, B.; Wang, S.Y.; Tang, C.A. Research on zonal disintegration characteristics and failure mechanisms of deep tunnel in jointed rock mass with strength reduction method. *Mathematics* **2022**, *10*, 922. [[CrossRef](#)]
27. Mazars, J.; Pijaudier-Cabot, G. Continuum damage theory-application to concrete. *J. Eng. Mech.* **1989**, *115*, 345–365. [[CrossRef](#)]
28. Wang, Y.Y.; Gong, B.; Tang, C.A. Numerical investigation on anisotropy and shape effect of mechanical properties of columnar jointed basalts containing transverse joints. *Rock Mech. Rock Eng.* **2022**, *55*, 7191–7222. [[CrossRef](#)]

29. Bahaaddini, M.; Sharrock, G.; Hebblewhite, B.K. Numerical investigation of the effect of joint geometrical parameters on the mechanical properties of a non-persistent jointed rock mass under uniaxial compression. *Comput. Geotech.* **2013**, *49*, 206–225. [[CrossRef](#)]
30. Nassir, M.; Settari, A.; Wan, R. Joint stiffness and deformation behaviour of discontinuous rock. *J. Can. Pet. Technol.* **2010**, *49*, 78–86. [[CrossRef](#)]
31. Zheng, B.W.; Qi, S.W.; Huang, X.L.; Guo, S.F.; Wang, C.L.; Zhan, Z.F.; Luo, G.M. An advanced shear strength criterion for rock discontinuities considering size and low shear rate. *Appl. Sci.* **2020**, *10*, 4095. [[CrossRef](#)]
32. Wang, X.; Yuan, W.; Yan, Y.T.; Zhang, X. Scale effect of mechanical properties of jointed rock mass: A numerical study based on particle flow code. *Geomech. Eng.* **2020**, *21*, 259–268.
33. Fan, X.; Kulatilake, P.; Chen, X. Mechanical behavior of rock-like jointed blocks with multi-non-persistent joints under uniaxial loading: A particle mechanics approach. *Eng. Geol.* **2015**, *190*, 17–32. [[CrossRef](#)]
34. Wu, N.; Liang, Z.Z.; Li, Y.C.; Qian, X.K.; Gong, B. Effect of confining stress on representative elementary volume of jointed rock masses. *Geomech. Eng.* **2019**, *18*, 627–638.
35. Zhou, J.X.; Zhou, Y.; Gao, Y.T. Effect mechanism of fractures on the mechanics characteristics of jointed rock mass under compression. *Arab. J. Sci. Eng.* **2018**, *43*, 3659–3671. [[CrossRef](#)]
36. Chen, G.Q.; Sun, X.; Wang, J.C.; Wang, D.; Zhu, Z.F. Detection of cracking behaviors in granite with open pre-cut cracks by acoustic emission frequency spectrum analysis. *Arab. J. Geosci.* **2020**, *13*, 258. [[CrossRef](#)]
37. Meng, F.Z.; Wong, L.N.Y.; Zhou, H.; Wang, Z.Q.; Zhang, L.M. Asperity degradation characteristics of soft rock-like fractures under shearing based on acoustic emission monitoring. *Eng. Geol.* **2020**, *266*, 105392. [[CrossRef](#)]
38. Guo, Q.F.; Pan, J.L.; Cai, M.F.; Zhang, Y. Investigating the effect of rock bridge on the stability of locked section slopes by the direct shear test and acoustic emission technique. *Sensors* **2020**, *20*, 638. [[CrossRef](#)] [[PubMed](#)]
39. Zhang, Y.C.; Jiang, Y.J.; Asahina, D.; Wang, Z. Shear behavior and acoustic emission characteristics of en-echelon joints under constant normal stiffness conditions. *Theor. Appl. Fract. Mech.* **2020**, *109*, 102772. [[CrossRef](#)]
40. Wang, G.; Zhang, Y.Z.; Jiang, Y.J.; Liu, P.X.; Guo, Y.S.; Liu, J.K.; Ma, M.; Wang, K.; Wang, S.G. Shear behaviour and acoustic emission characteristics of bolted rock joints with different roughnesses. *Rock Mech. Rock Eng.* **2018**, *51*, 1885–1906. [[CrossRef](#)]